

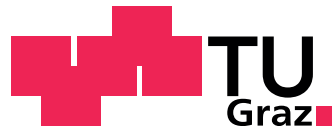
Markus Krug

Bright and Dark Plasmonic Modes of Silver Nanodisks

MASTER THESIS

For obtaining the academic degree
Diplom-Ingenieur

Master Programme of
Technical Physics



Graz University of Technology

Supervisor:

Univ.-Prof. Dr. Joachim R. Krenn

Institute of Physics
Karl-Franzens-University Graz

Graz, January 2014

Deutsche Fassung:
Beschluss der Curricula-Kommission für Bachelor-, Master- und Diplomstudien vom 10.11.2008
Genehmigung des Senates am 1.12.2008

EIDESSTÄTTLICHE ERKLÄRUNG

Ich erkläre an Eides statt, dass ich die vorliegende Arbeit selbstständig verfasst, andere als die angegebenen Quellen/Hilfsmittel nicht benutzt, und die den benutzten Quellen wörtlich und inhaltlich entnommenen Stellen als solche kenntlich gemacht habe.

Graz, am

.....
(Unterschrift)

Englische Fassung:

STATUTORY DECLARATION

I declare that I have authored this thesis independently, that I have not used other than the declared sources / resources, and that I have explicitly marked all material which has been quoted either literally or by content from the used sources.

.....
date

.....
(signature)

meinen Eltern

Abstract

Metallic nanoparticles display unique optical properties that arise from resonant coupling of the conduction electrons to incident light, i.e., plasmon modes. The important role of the nanoparticle shape implies a tunability of the resonance frequencies of the fundamental dipole and higher order modes. We distinguish between optically bright modes that couple to incident light via their dipole moments, and dark modes which possess no dipole moments. For silver nanodisks, a rich variety of plasmon modes is known but only recently a new mode has been found by electron energy loss spectroscopy. This excitation is termed breathing mode because of the radially symmetric charge density oscillations, whose vanishing dipole moment is the reason why it usually does not couple to light and so far has escaped optical observation.

In this work we use electron beam lithography to fabricate silver nanodisks. Relying on optical spectroscopy, the bright and dark modes of nanodisks are studied with a focus on identifying the plasmonic breathing mode. Therefore, we make use of field retardation and symmetry breaking by illumination at oblique incidence. Indeed, due to their finite spatial extent, dark nanodisk modes are accessible by far field illumination. The measurements are accompanied by numerical simulations to corroborate the findings. Furthermore, we apply the results of the optical characterization to build a hybrid plasmonic structure from silver nanodisks and semiconducting colloidal quantum dots and demonstrate the coupling of nanodisks and emitters using fluorescence lifetime measurements.

Kurzfassung

Metallische Nanopartikel zeigen durch die Möglichkeit der resonanten Kopplung der Leitungselektronen mit Licht einzigartige optische Eigenschaften, die auf plasmonische Moden zurückzuführen sind. Die Resonanzfrequenzen der fundamentalen Dipolmode und die der Moden höherer Ordnung hängen dabei von der Form der Nanopartikel ab. Wir unterscheiden zwischen strahlenden Moden (bright modes), die über ihr Dipolmoment mit einfallendem Licht wechselwirken, und dunklen Moden (dark modes), die kein Dipolmoment aufweisen. Für Nanoscheiben ist bereits eine Anzahl an unterschiedlichen Plasmonenmoden bekannt, jedoch wurde erst kürzlich mittels Elektronenenergieverlust-Spektroskopie eine neue Plasmonenmode entdeckt. Der englische Name *breathing mode* rührt von den charakteristischen radialsymmetrischen Oszillationen der Ladungsdichte her, auf deren verschwindendes Dipolmoment es zurückzuführen ist, dass die Mode bis jetzt mit optischen Methoden unentdeckt blieb.

In dieser Arbeit untersuchen wir die strahlenden und dunklen Plasmonenmoden von elektronenstrahlolithographisch hergestellten Nanoscheiben mit optischen Spektroskopiemethoden. Hierzu machen wir uns Retardierungseffekte und einen Symmetriebruch durch die Beleuchtung unter schrägem Einfallswinkel zunutze und richten besonderes Augenmerk auf die neu entdeckte radialsymmetrische Mode. Wir zeigen, dass durch die Größe der untersuchten Scheiben eine optische Anregung der dunklen Moden aus dem Fernfeld möglich ist. Unterstützend zu den Messungen werden numerische Simulationen durchgeführt, welche die Ergebnisse bekräftigen. Anschließend verwenden wir die erhaltenen Ergebnisse um Nanoscheiben aus Silber mit halbleitenden kolloidalen Quantenpunkten zu kombinieren. Dabei können wir durch eine deutlich verringerte Fluoreszenzlebensdauer der Quantenpunkte auf eine Kopplung rückschließen.

Contents

1. Introduction	1
2. Theory	5
2.1. The dielectric function	5
2.2. Particle plasmons	8
2.3. Quantum dots	11
2.4. Electromagnetic near- and far-field	12
2.5. Interaction of emitters and plasmonic structures	13
3. Fabrication and characterization	16
3.1. Electron beam lithography	16
3.2. Spectroscopy of nanoparticle arrays	21
3.3. Single particle spectroscopy	24
3.4. Fluorescence spectroscopy	29
3.5. Time correlated single photon counting	31
3.6. Numerical simulation of plasmonic nanoparticles	34
4. The mode spectrum of plasmonic nanodisks	38
4.1. Electron energy loss spectroscopy of nanodisks	38
4.2. Optical spectroscopy of nanodisk arrays	42
4.3. Plasmonic edge and film modes	54
4.4. Optical spectroscopy of single nanodisks	57
5. Coupling of quantum dots and nanodisks	61
5.1. Fabrication of hybrid structures	61
5.2. Spectroscopy of hybrid structures	62
5.3. Fluorescence lifetime measurements	69
6. Conclusion	74
Bibliography	77
A. Appendix	81
A.1. Fabrication parameters	81
A.2. Sample characterization	83

1. Introduction

Today's strive for miniaturization of devices and advances in fabrication methods have led to the rise of *nanotechnology*, a research field concerning matter with structural sizes below 100 nm. This length-scale is not accessible for conventional optics, as the Abbé diffraction limit does not allow to focus light to dimensions smaller than about half the wavelength. This poses serious limitations for the fundamental study of the interaction of light and matter when relying on optical instruments as well as for technological applications where information processing and transport is strongly based on optical technology.

However, light does not only exist as propagating waves, but also occurs as evanescent fields that are bound to surfaces and extend over distances corresponding to a fraction of the wavelength. For these *near-fields* the diffraction limit is not relevant and light can be spatially modulated arbitrarily, in principle even by the atomic structure of the surface. Optical near-fields exist around all scattering objects or sources of light, and they are actually probed to circumvent the diffraction limit in near-field optical microscopy. However, methods to control and efficiently create these near-fields are needed. Metallic nanoparticles turn out to be ideal candidates for this purpose as they support collective oscillations of the conduction electrons that interact resonantly with incoming light. The oscillating charges of this *particle plasmons* generate strong near-fields, that can be considerably stronger than the exciting light fields. Importantly, due to the small size of the particles, light is effectively squeezed into sub-wavelength volumes. This enables metal-based nano-optics beyond the diffraction limit, a field that is termed *plasmonics* [1]. The technological promises of plasmonics range from sensing applications [2] to the hope that the small size combined with the high optical frequencies may bridge the gap between nanometer sized electronic components and the current micrometer size of optical waveguides [3] or even replace them entirely with miniaturized integrated photonic circuits [4].

The particle plasmon resonance frequency depends on the used material (commonly gold or silver because of their relatively low Ohmic losses) and on the geometry of the particle. Incident light that matches the resonance

frequency is strongly scattered or absorbed in the particle. By changing the axis ratio of metallic particles, the resonance can be tuned throughout the visible and near-infrared spectral range.

For resonant plasmonic modes, analogies to mechanical vibrations can be drawn. First, the shape of a vibrating body has an effect on the resonance frequency. Second, similarly to normal modes of mechanical vibrations (higher harmonics), more than one resonance frequency can exist for a given shape. In plasmonic structures the fundamental mode is a displacement of the electron cloud that leads to surface charges with dipolar character. The higher order modes are characterized by their respective symmetries of the electron density oscillations. However, like the vibrations of specific mechanical modes depend on the excitation – a drum has a different sound depending on how it is struck – not all plasmonic modes can be excited by incident optical plane waves.

Because of its inherent symmetry, a plane wave can only couple resonantly to plasmonic modes with a net-dipole moment, such as the fundamental dipole mode. As such modes can be observed with optical methods, e.g., in dark field microscopy, they are termed *bright*. However, other plasmon modes of higher symmetry do not necessarily have a dipole moment and therefore do not couple to light. These modes are optically *dark* for sufficiently small nanoparticles.

Electron energy loss spectroscopy (EELS) is a technique that measures losses of an electron beam that has passed a sample. The fact that electrons lose kinetic energy to plasmonic excitations can be used to create detailed spatial maps of plasmonic modes when EELS is implemented in an electron microscope. As the interaction of an electron beam and plasmonic modes does not rely on a dipole moment, it can be used to probe the complete plasmonic mode spectrum of metallic nanoparticles, including bright and dark modes.

Nanodisks are known to support a variety of bright and dark multipolar plasmonic modes, nevertheless, recent EELS studies have shown a previously undiscovered dark plasmonic mode. Due to its radially symmetric charge distribution it was termed breathing mode [5]. In the context of nano-optics it seems natural to attempt an optical characterization of the full plasmonic mode spectrum, to find conditions under which dark modes of silver nanodisks can be excited. Here, special emphasis is placed on the dark plasmonic breathing mode, which so far has only been observed with the EELS technique. In general, dark plasmonic modes are interesting because the vanishing dipole results in a reduction of radiation losses, which suggests that dark modes store electromagnetic energy better than bright modes.

This can be used to create lossless plasmon waveguides [6] and makes them attractive in respect to their application for optical cavities with high quality factors that might enable surface-plasmon lasing [7].

The optical characterization in this work is done by using two complementary spectroscopic techniques: transmission measurements of particle arrays and scattering spectroscopy of single nanoparticles. When it comes to optical far-field excitation and detection of dark plasmon modes there are different approaches that rely on symmetry breaking. One possibility is to use Fano resonances by coupling a dark to a bright mode [8] [9]. A different method, which is used in this work, is to deploy *retardation* effects. This requires that the nanoparticles are large enough, so that the quasi-static approximation is not valid anymore. When light is incident at an oblique angle, the electric field can be non-uniform across the nanoparticle. This opens up the possibility to exert higher order moments on the conduction electrons so that dark plasmon modes can be excited [10] [11].

The spectroscopic measurements are accompanied by numerical simulations with the MNPBEM¹ toolkit [12] to understand the optical spectra. In addition, we relate the optical results to the EELS data, by considering the respective dispersion relations. We complement the optical characterization with single particle spectroscopy, a technique that analyzes scattered light from single nanodisks and allows to deduce variations between single lithographically fabricated particles.

Finally, relying on the results obtained by optical spectroscopy, the coupling of quantum dots – placed on the silver nanodisks – to the plasmonic breathing mode is considered. On the one hand the presence of plasmonic nanostructures gives rise to additional decay channels for the quantum dots, on the other hand the rapidly varying near-fields of the emitters placed in close vicinity of nanostructures break the symmetry so that dark modes can be excited [13]. From the EELS study it is known that from all plasmonic modes on silver nanodisks, the plasmonic breathing mode couples strongest to the electron beam. This can be explained by the small radiation losses of dark modes and the associated low damping which leads to strong local fields and should signify an efficient interaction with nearby quantum dots.

Because of the finite size of the nanodisks, the breathing mode is not completely dark. A radiative decay of the breathing mode could lead to spectral shaping of the quantum dot emission [14] which we aim to identify. As another approach to assess this hybrid system, we use fluorescence lifetime measurements. The presence of plasmonic structures introduces additional decay channels which lead to changes in fluorescence lifetime.

¹metal nanoparticle boundary element method

Thesis structure

In chapter 2 the concept of plasmonic excitations is introduced, which is crucial to understand the optical properties of metallic nanostructures. Furthermore, quantum dots are reviewed in respect to their application as elementary emitters and to their interactions with plasmonic structures. In chapter 3, the tailored fabrication of nanostructures, their optical characterization and the basics of their numerical simulation are explained. After a brief discussion of electron energy loss spectroscopy results that are relevant for this work, chapter 4 is dedicated to the optical characterization of nanoparticle arrays, corroborated by numerical simulations. These findings are applied to build coupled plasmonic structures that are optically analyzed in chapter 5. The results are summarized in the conclusion, chapter 6, adjoining are the perspective and the acknowledgment section. Supplementary information concerning sample fabrication is covered in the appendix.

2. Theory

2.1. The dielectric function

The dielectric function $\varepsilon(\omega)$ governs the electrical and optical properties of a material for a certain angular frequency ω . It is defined as the relation between electric displacement \mathbf{D} – which describes the response of free and bound charges in a material – and an applied electric field \mathbf{E} , according to the following constitutive equation:

$$\mathbf{D}(\omega) = \varepsilon_0 \varepsilon(\omega) \mathbf{E}(\omega). \quad (2.1)$$

This relation, wherein ε_0 is the vacuum permittivity, is valid for an isotropic material. In general, the dielectric function is a complex, frequency dependent quantity:

$$\varepsilon(\omega) = \varepsilon_1(\omega) + i\varepsilon_2(\omega). \quad (2.2)$$

The dielectric function can be used to deduce optical quantities, such as polarizability or reflectivity. This becomes clear by its direct relation to the complex refractive index $N = n + ik$, in which n is the refractive index, and k the absorption coefficient:

$$\varepsilon(\omega) = N^2. \quad (2.3)$$

A simple deduction of the dielectric function for metals can be done by the Drude model, where free electrons move against stationary, positive ions. Despite its simplicity, this model can be used to explain the optical properties of metals for a broad range of frequencies [15]. The approach starts from the equation of motion for a single electron in an external electric field \mathbf{E} , the complete derivation can be found in Ref. [16]:

$$m\ddot{\mathbf{x}} + m\gamma\dot{\mathbf{x}} = -e\mathbf{E} \quad (2.4)$$

The damping constant γ is the inverse of the collision time τ , m and e are the mass and the charge of one electron, respectively. This equation is solved

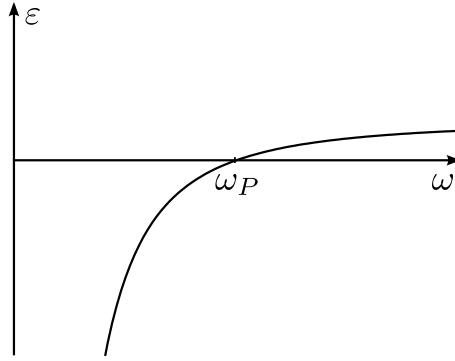


Figure 2.1.: Schematic dielectric function for a Drude metal in the limit of zero damping.

for the displacement \mathbf{x} of the electron:

$$\mathbf{x}(t) = \frac{e}{m(\omega^2 + i\gamma\omega)} \mathbf{E}(t), \quad (2.5)$$

which can then be used to express the macroscopic polarization $\mathbf{P} = -n e \mathbf{x}$, n being the number of electrons. By inserting the polarization into the expression for the electric displacement field $\mathbf{D} = \varepsilon_0 \mathbf{E} + \mathbf{P}$, we arrive at:

$$\mathbf{D} = \varepsilon_0 \left(1 - \frac{\omega_p^2}{\omega^2 + i\gamma\omega} \right) \mathbf{E}. \quad (2.6)$$

Here, the natural frequency $\omega_p = \frac{ne^2}{\varepsilon_0 m}$ appears, which is the plasma frequency of the electron gas. Finally, by comparing with Eq. 2.1, the following expression for the dielectric function is obtained:

$$\varepsilon(\omega) = 1 - \frac{\omega_p^2}{\omega^2 + i\gamma\omega}. \quad (2.7)$$

In the limit of zero damping ($\tau \rightarrow \infty$) the dielectric function is real and can be written as:

$$\varepsilon(\omega) = 1 - \frac{\omega_p^2}{\omega^2}. \quad (2.8)$$

This dielectric function is plotted schematically in Fig. 2.1. To discuss the meaning of the plasma frequency ω_p in the dielectric function, we consider

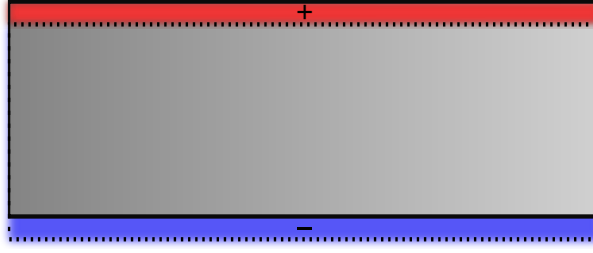


Figure 2.2.: Sketch of the volume plasmon, the colored regions correspond to resulting (oscillating) surface charges.

plane waves as solutions of the wave equation:

$$\mathbf{E} = \text{Re}[\mathbf{E}(\omega) \exp(i(\mathbf{k}\mathbf{r} - \omega t))], \quad (2.9)$$

with the following dispersion relating the wave vector \mathbf{k} with ω :

$$\mathbf{k}^2 = \frac{\varepsilon(\omega)\omega^2}{c^2}. \quad (2.10)$$

Inserting the dielectric function $\varepsilon(\omega)$ from Eq. 2.8 into the dispersion relation and further into the plane wave form, three different cases can be distinguished:

- for $\omega < \omega_p \Rightarrow \varepsilon < 0$, the wave vector \mathbf{k} becomes complex. Here, an exponentially decaying wave is obtained, i.e., an incoming electromagnetic wave is reflected. This is metallic behavior.
- for $\omega > \omega_p \Rightarrow \varepsilon > 0$, \mathbf{k} is real. The result is a propagating transverse electromagnetic wave. The metal is transparent in this frequency regime and has dielectric character.
- for $\omega = \omega_p \Rightarrow \varepsilon = 0$, \mathbf{k} vanishes. This is a longitudinal non-propagating wave that is characterized by being a pure depolarization field [16].

If free electrons in a metal are displaced at one instant in time, all electrons will oscillate back and forth in phase against the positive ions with the plasma frequency ω_p , see Fig. 2.2. This oscillation cannot couple to transverse electromagnetic waves, it can only be excited upon charged particle impact. The quasiparticle of this plasma excitation is the volume (or bulk) plasmon.

When we consider surfaces, another plasmon type can exist. Surface plasmons (SPs) are propagating waves at metal/dielectric interfaces, where an

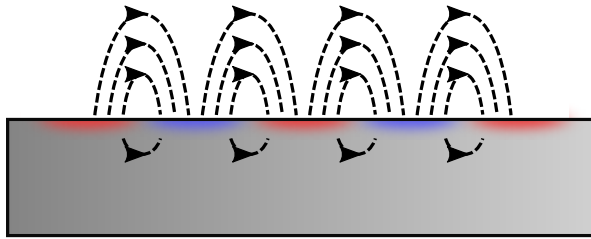


Figure 2.3.: Sketch of a surface plasmon. The colored region correspond to the positive and negative space charge densities, the arrows indicate the electric field.

electromagnetic field is coupled to density oscillations of the electron plasma. A graphical representation of this plasma excitation is shown in Fig. 2.3. Due to the hybrid character, surface plasmons are evanescently confined and localized to the interface. The possible frequency range is from 0 to $\omega_p/\sqrt{2}$ [16].

To make a transition from an extended surface to a nanoparticle, we can think of first moving from a two dimensional surface to a quasi one-dimensional wire, by rolling up the metal/dielectric interface. The plasmon are be guided by the wire. Because of the new periodic boundary condition, the charge oscillation around the wire has to be periodic. This implies a partitioning of the field over the circumference of the wire, which leads to discrete plasmonic modes with specific frequencies [7].

2.2. Particle plasmons

We now discuss localized particle plasmons as non-propagating excitations of the conduction electrons that are resonantly interacting with an incoming electromagnetic field. As briefly sketched above for the one-dimensional plasmonic wire, for particles we expect discrete charge oscillations, similar to standing waves.

In the following, we make the assumption that all particle dimensions d are much smaller than the wavelength of the incoming light wave, $d \ll \lambda$. This is known as the quasi-static approximation, because the phase of the oscillating electric field is constant across the particle for any instant in time. The fundamental particle plasmon excitation is a dipole-like mode. As it can be seen from Fig. 2.4, the electron cloud is displaced to one side, which results in an accumulation of surface charges. This introduces a restoring force between the negatively charged electrons and the positive ion cores,

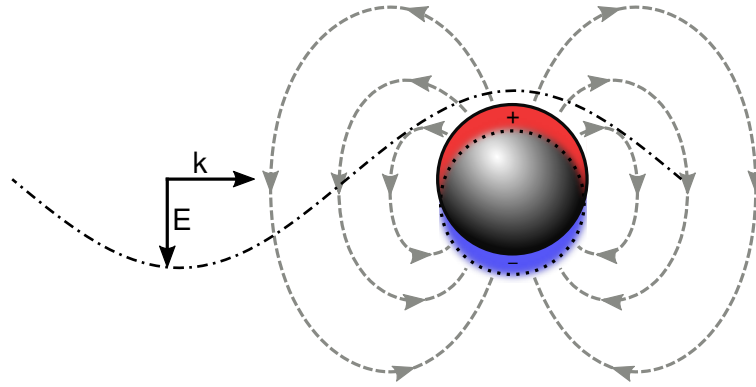


Figure 2.4.: Sketch of a particle plasmon. The electron displacement within a metal sphere is resonant with an incident light wave, characterized by its wave vector \mathbf{k} and the electric field vector \mathbf{E} . The displacement gives rise to surface charges (colored regions) which constitute an oscillating electric dipole. Its electric near-field is sketched with the dashed lines.

where the restoring force determines the resonance frequency.

For spheres in the quasi-static approximation, the calculation of the resonance frequency is straightforward as retardation effects can be ignored and the incident plane wave can be approximated by a constant electric field $\mathbf{E} = E_0 \hat{\mathbf{z}}$ [16]. In the following discussion, a is the radius and $\varepsilon(\omega)$ the dielectric constant of the sphere, ε_m is the dielectric constant of the surrounding medium. This problem involves the solution of the Laplace equation $\nabla^2 \Phi = 0$, from which the electric field $\mathbf{E} = -\nabla \Phi$ can be calculated. Because of the azimuthal (θ) symmetry, the potential Φ can be written in terms of Legendre polynomials P_l [17]:

$$\Phi(r, \theta) = \sum_{l=0}^{\infty} (A_l r^l + B_l a^{-(l+1)}) P_l(\cos \theta). \quad (2.11)$$

From the boundary conditions for the sphere, the coefficients (A_l , B_l) for the respective Legendre polynomials can be calculated. It can be shown that for constant electric field only the coefficients for the first Legendre polynomial $l = 1$ are depending on the electric field [7]. The resulting potential outside the sphere can be written as [16]:

$$\Phi_{out} = -E_0 r \cos \theta + \frac{\boldsymbol{\mu} \cdot \mathbf{r}}{4\pi \varepsilon_0 \varepsilon_m r^3}, \quad (2.12)$$

where a dipole moment $\boldsymbol{\mu}$ appears that is proportional to the applied field,

$$\boldsymbol{\mu} = 4\pi\varepsilon_0\varepsilon_m a^3 \frac{\varepsilon - \varepsilon_m}{\varepsilon + 2\varepsilon_m} \mathbf{E}_0, \quad (2.13)$$

i.e, the complex polarizability α according to

$$\boldsymbol{\mu} = \varepsilon_0\varepsilon_m \alpha \mathbf{E}, \quad (2.14)$$

is given by:

$$\alpha = 4\pi a^3 \frac{\varepsilon - \varepsilon_m}{\varepsilon + 2\varepsilon_m}. \quad (2.15)$$

If the denominator $|\varepsilon + 2\varepsilon_m|$ is a minimum, there is a resonance and the polarizability is maximum. For a slowly-varying imaginary part $\text{Re}[\varepsilon]$ this condition becomes:

$$\text{Re}[\varepsilon(\omega)] = -2\varepsilon_m. \quad (2.16)$$

This is the so-called *Fröhlich* condition for the dipole mode [16]. For the Drude dielectric function described in Eq. 2.8 and $\varepsilon_m = 1$ in air, the resonance frequency of the electric field is $\omega_0 = \omega_p/\sqrt{3}$. This result signifies that the resonance frequency of a sphere is independent of the radius a in the quasi-static approximation.

From the polarizability α , the absorption cross section C_{abs} and the scattering cross section C_{sca} can be calculated [18]:

$$C_{sca} = \frac{k^4}{6\pi} |\alpha|^2 = \frac{8\pi}{3} k^4 a^6 \left| \frac{\varepsilon - \varepsilon_m}{\varepsilon + 2\varepsilon_m} \right|^2 \quad (2.17)$$

$$C_{abs} = k \text{Im}[\alpha] = 4\pi k a^3 \text{Im} \left[\frac{\varepsilon - \varepsilon_m}{\varepsilon + 2\varepsilon_m} \right] \quad (2.18)$$

The absorption cross section C_{abs} scales with the volume $V \propto a^3$ of the particle, the scattering cross section C_{sca} grows with $V^2 \propto a^6$. This means that for small particles $d \ll \lambda$, light is mainly absorbed, but for larger particles scattering becomes predominant.

2.2.1. Multipolar plasmonic modes

Until now, only the fundamental dipole mode has been considered. In the calculation for the resonance condition of a sphere, for constant electric field \mathbf{E}_0 the higher order Legendre polynomials $l > 1$ did not contribute to the

solution. In fact, these terms correspond to higher order modes [7].

The physical interpretation is that such modes do not possess a net-dipole moment but instead higher order (e.g., quadrupole) moments, which cannot interact with an electric field that is constant across the sphere, as it results from an incoming plane wave in the quasi-static approximation. Modes with no dipole moment are thus so-called *dark* modes. However, outside the quasi-static approximation, when phase retardation must be considered, an incident plane wave can transfer higher order moments, so that multipolar modes can be excited. This can already be the case if particle dimensions are 10% of the wavelength of the incident light [7].

For spheres and spheroids of arbitrary size, the optical response can be calculated with classical Mie-theory [19]. It represents an exact solution of Maxwell's equations, i.e., including retardation, using boundary conditions in spherical coordinates and multipole series expansion of the incident electro-magnetic field [20]. With Mie-theory, scattering and absorption spectra that take into account higher order multipolar modes, such as the quadrupole mode, can be calculated.

However, for arbitrary particle shapes, e.g., electron beam lithography fabricated structures (see section 3.1), Mie-theory cannot be solved analytically, and, thus, numerical methods are needed. Also, for new spectroscopic techniques, such as surface-enhanced Raman spectroscopy not only the optical far-field response, but also the electric near-fields are of interest. This strongly motivated the development for numerical methods [21]. This is also true for electron energy losses in EELS (see section 4.1). The numerical method used in this work is discussed in section 3.6.

2.3. Quantum dots

Quantum dots (QDs) are nanocrystals from semiconductor materials, that exhibit quantum mechanical properties due to their small size of typically 2–10 nm. In the context of this work, they are mainly used because of their unique properties as fluorescent dyes, such as excellent photostability and strong dipole moment. In a semiconductor, an absorbed photon with an energy $\hbar\omega$ larger than the bandgap E_g can lift an electron from the valence band into the conduction band. The electron and the hole are attracted by Coulomb force and constitute an electron-hole-pair known as exciton, see Fig. 2.5 a). The quasi-particle of this bound state is characterized by its exciton Bohr radius, which depends on the semiconductor material. When the size of the semiconductor becomes smaller than its respective exciton Bohr

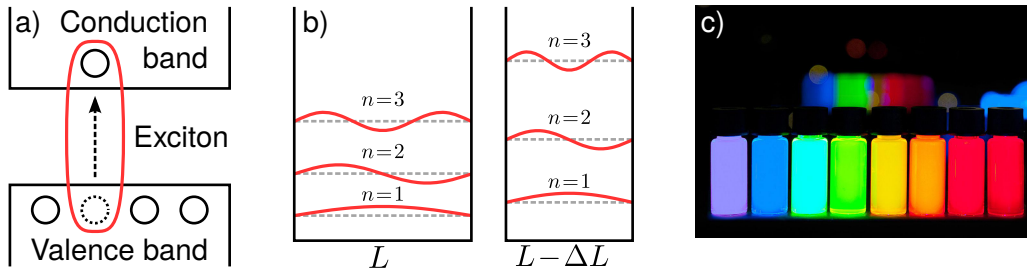


Figure 2.5.: Properties of QDs: a) When an electron is lifted into the conduction band it still interacts with the created hole in the valence band, forming an exciton. b) The size effect of quantum confinement can be understood in terms of a particle-in-a-box model, where reducing the width (L) of an infinite potential well increases the discrete (n) energy levels. This leads to a tunable emission wavelength as shown for c) ZnCdSeS QDs¹.

radius, the wavefunctions of the carriers – electrons and holes – experience quantum confinement. As a consequence, the carrier energies are at discrete energies.

For smaller QDs the difference between the discrete energy levels increases, similarly to the quantum mechanical particle-in-a-box model in Fig. 2.5 b). As a consequence, the difference between hole energies and electron energies is increased, which means that the photons that are involved in the creation and recombination of carriers have higher energies. This implies that optical properties, such as the emission wavelength, can be tuned with the nanocrystal size as shown in Fig. 2.5 c).

2.4. Electromagnetic near- and far-field

These notions describe regions around electromagnetic sources such as oscillating electric dipoles or scattering objects. Roughly speaking, the near-field constitutes the region $r < \lambda$ and the far-field is the region $r > \lambda$.

In close vicinity of the source, there are no restrictions on the electromagnetic field components and, therefore, arbitrary wave vectors can occur. However, not all of these wave vectors are propagable. There exists a cut-off wave vector $k_0 = 2\pi/\lambda$, so that fields with larger wave vectors decay exponentially within a fraction of the wavelength. This constitutes the non-

¹Image taken by Wikipedia user Antipoff, licensed under CC BY-SA 3.0.

radiative near-field. On the other hand, the propagating components travel into the far-field region as plane waves and the according field decays with $1/r^2$.

With regard to particle plasmons, we have discussed in section 2.2 that bright modes couple to plane waves via their dipole moment. Disregarding field retardation (i.e., for small particles in the quasi-static approximation) the symmetry of plane waves makes it impossible to couple to dark plasmonic modes. However, emitters such as QDs, can be described as oscillating electric dipoles [17]. The electric field components in their near-field can provide the appropriate (large) wave vectors that permit a coupling to plasmonic dark modes. This requires the placement of QDs in vicinity of the plasmonic structure.

2.5. Interaction of emitters and plasmonic structures

In this section we treat the effects of the strong near-fields of plasmonic nanostructures on linear optical processes in emitters. Plasmonic structures can have an effect on the absorption and emission properties of an emitter in their vicinity. For absorption, the strong near-field of the metal nanoparticle has the same effect as increasing the intensity of the incident light. This directly leads to an absorption enhancement if the emitter is not already saturated. The metal nanoparticle can be seen as an antenna that increases the absorption cross section of the emitter. In the context of this work, we are more concerned about the enhancement of the spontaneous emission by metal nanoparticles. The spontaneous emission rate Γ_r is described by Fermi's golden rule [22]:

$$\Gamma_r = \frac{2\pi}{\hbar} \left| \langle g | \hat{\boldsymbol{\mu}} \cdot \hat{\mathbf{E}} | e_1 \rangle \right|^2 \rho(\omega), \quad (2.19)$$

with the electric dipole operator $\hat{\boldsymbol{\mu}}$ and the electric field operator $\hat{\mathbf{E}}$. The expression $\left| \langle g | \hat{\boldsymbol{\mu}} \cdot \hat{\mathbf{E}} | e_1 \rangle \right|^2$ is the transition matrix element which is a measure for the transition probability between the first excited state $|e_1\rangle$ and the ground state $|g\rangle$. The scalar product signifies that the relative orientation of the dipole is taken into account.

The spontaneous emission rate Γ_r is directly proportional to the local density of states (LDOS) $\rho(\omega)$. The mechanism of the emission enhancement through metallic nanoparticles is by increasing the LDOS. This is analogous

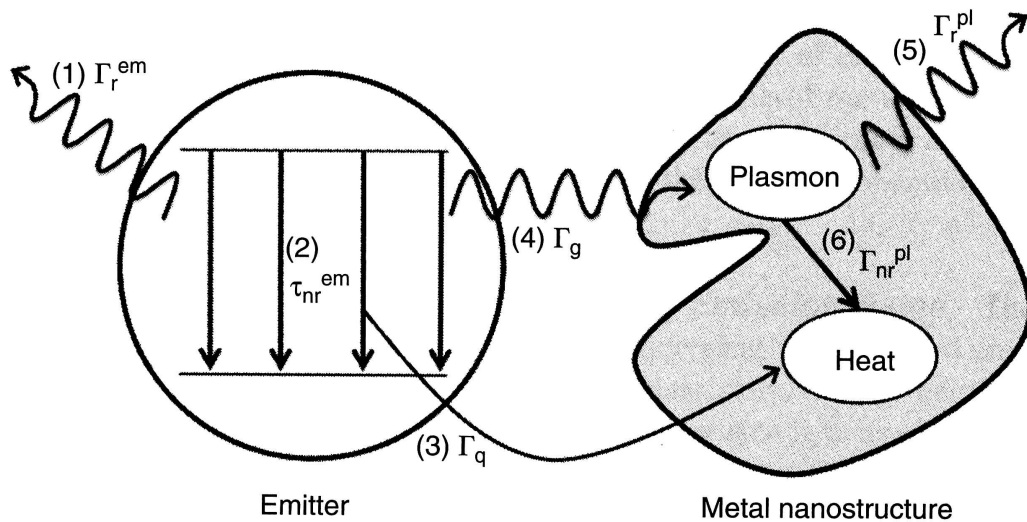


Figure 2.6.: Schematic of the possible processes in a coupled emitter-plasmon system in terms of their respective rates Γ . (1) and (2) are radiative (r) and non-radiative (nr) decays of the emitter, (3) is luminescence quenching due to the presence of the metal. (4) is a decay process of the emitter that involves the excitation of plasmons. These plasmonic excitations then can decay radiatively (5) or non-radiatively (6). From Ref. [7].

to the increased optical mode density in optical cavities, with the cavity mode of the optical resonator being replaced by the plasmon resonance of the nanoparticle. For an extensive review, see Ref. [23].

Figure 2.6 provides an overview of the different decay rates in a coupled emitter-plasmon system. The emitter can decay radiatively by emission of a photon into the far-field with the rate Γ_r^{em} , where the superscript “em” denotes the emitter. It can also relax in a non-radiative process with the respective rate Γ_{nr}^{em} . A different set of non-radiative decays is due to either non-plasmonic excitations in the metal or charge transfer (Ohmic damping). This is called (luminescence) *quenching* and is taken into account by the rate Γ_q . Finally, the emitter can excite plasmon excitations within the metal nanoparticle with a rate Γ_g .

From the two far-field emission rates we can calculate the spontaneous emission enhancement due to the presence of plasmonic nanostructures, de-

scribed by the *Purcell* factor F_P :

$$F_P = \frac{\Gamma_g + \Gamma_r^{em}}{\Gamma_r^{em}} = 1 + \frac{\Gamma_g}{\Gamma_r^{em}}. \quad (2.20)$$

The total relaxation rate is the sum over all decay processes:

$$\Gamma_{tot} = \Gamma_g + \Gamma_r^{em} + \Gamma_{nr}^{em} + \Gamma_q. \quad (2.21)$$

While this total relaxation rate is relatively easy to measure experimentally, its interpretation is often not obvious, because it is composed of several rates that are difficult to separate. In Fig. 2.6 the plasmon related decay times are indicated as well. In general, they are much faster than the relaxation times related to the emitter. There is a radiative process Γ_r^{pl} and a non-radiative decay Γ_{nr}^{pl} .

Apart from the changing absorption, emission and relaxation rates, the interaction with plasmonic structures can appear in several other effects. An example is the modification of the emission spectrum by coupling to the plasmonic structure. Emitters often have a multitude of overlapping transitions that result in broadened emission spectra. If the plasmon mode is spectrally narrow compared to the emission spectrum of the emitter, the coupling can result in a selection of certain resonant frequencies and a suppression of others. If the emitter is strongly coupled to the radiatively decaying plasmon, the emission spectrum will resemble that of the coupled plasmonic mode.

A different aspect concerns the emission pattern. When the emitter excites a plasmon that decays radiatively, the radiation pattern will be that of the plasmon mode. Again, when the coupling to a radiative plasmon mode is strong, the total far-field emission of the system will resemble that of the plasmonic mode.

3. Fabrication and characterization

3.1. Electron beam lithography

Electron beam lithography (EBL) is a technique for micro- and nanofabrication. A focussed electron beam is moved across an electron sensitive resist to *expose* a certain pattern, changing the solubility of the resist (usually by cracking molecular bonds in polymer chains) so that it can be selectively removed in a chemical *development* step. The result is a so-called mask, that can be used to either modify the non-protected substrate area by etching or ion implanting or to deposit some material. The mask can be dissolved later in a *lift-off* process step.

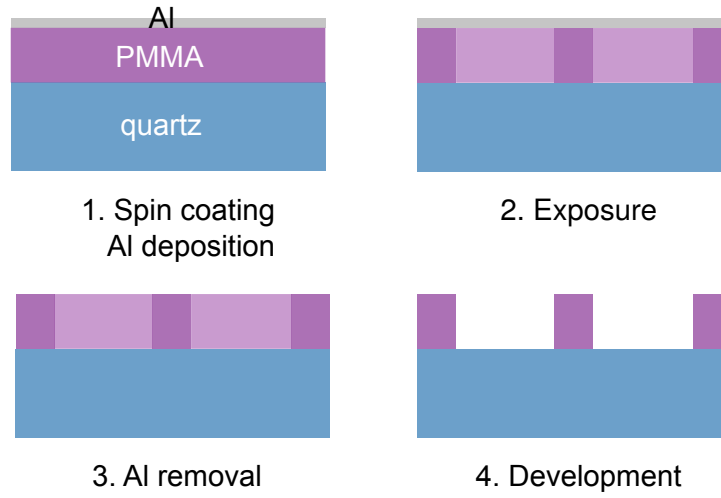
Electron beam lithography outperforms optical lithography as used in today's semiconductor device fabrication in terms of spatial resolution. This is because the de Broglie wavelength of fast electrons is much smaller than the wavelength of the light used for optical lithography. However, the achieved resolution of sub 10 nm in EBL is primarily limited by the forward scattering of the electrons and the outreach of the generated secondary electrons in the resist [24].

A fundamental difference of EBL and optical lithography is that the patterns in optical lithography are exposed at once (by projection), whereas the electron beam scans across the surface and writes in a sequential manner, which requires more time. The fact that EBL is a maskless lithography technique in combination with its high spatial resolution makes it the perfect fabrication technique for the low volume rapid-prototyping approach in nanotechnology research environments.

3.1.1. Fabrication of nanostructures with electron beam lithography

The sample preparation steps in EBL are depicted in Fig. 3.1 and discussed in the following. The corresponding process parameters are put together in appendix section A.1. The first part (A) is the mask fabrication, it is subsequently used to either fabricate metallic nanostructures (B) or to deposit colloidal nanoparticles (C).

A. Electron beam lithography



B. Metallic nanostructures

C. Colloidal nanoparticles

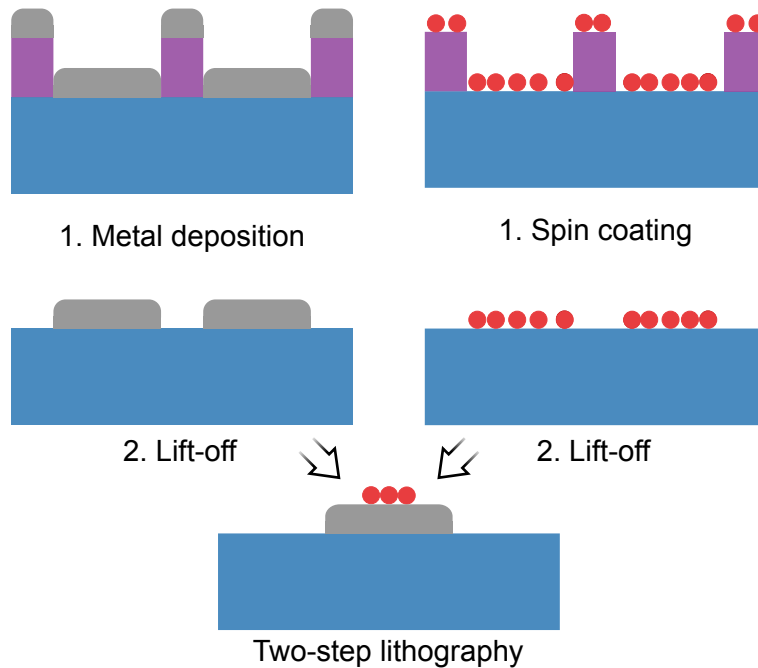


Figure 3.1.: Schematic of the sample preparation steps by means of EBL: (A) The EBL process is used to write a pattern into an electron beam resist (PMMA), which can then be used to (B) create metallic nanostructures or (C) position colloidal nanoparticles, such as QDs. The fabrication steps can be combined to create complex nanostructures as shown at the bottom.

A. Electron beam lithography

1. First, a (quartz or glass or ITO¹-glass) substrate is cut to the desired shape and cleaned according to the cleaning procedure (appendix section A.1.1). Then, after a N₂ plasma-cleaning step, the poly(methyl methacrylate) (PMMA) resist is spin coated onto the substrate. The thickness of the obtained resist film is typically 100 nm. The next step is the *pre-exposure bake*, where the substrate is heated well above the glass temperature of the PMMA. This baking step serves several purposes [25], e.g., it removes the solvent and it anneals and densifies the resist by removing small voids in the PMMA film [26]. This step is not critical and may be omitted if silver nanostructures are already present, otherwise they could be damaged.

If a conductive substrate, e.g., ITO covered glass, is used, we can proceed with step 2., if not, an 8 nm aluminum film is deposited onto the resist. This prevents electrostatic charging during the following exposure step.

2. For the exposure, the sample is transferred into the Raith e-line² EBL system. The shape of the focused electron beam is subsequently optimized, adjusting focus, astigmatism and beam alignment, and the correct exposure dose is set. In the actual exposure step, the electron beam scans across the sample, exposing the programmed pattern. This can take from a few minutes to several hours, depending on the pattern.
3. After the exposure, the conductive aluminum film (if present) is removed with diluted sodium hydroxide (NaOH) solution. This is done by either putting a drop onto the sample, or immersing the sample completely for a few seconds. The sample is subsequently rinsed with deionized water.
4. In the development step, the sample is submerged in a dedicated solvent. For so-called *positive-tone* photoresists such as PMMA, the exposed parts have a higher solubility than the unexposed parts and, thus, are removed. We finally have transferred a pattern into the PMMA film and can proceed.

¹indium tin oxide

²<http://www.raith.com>

B. Fabrication of metallic nanostructures

1. Metallic nanostructures are created by thin film deposition. The metal is thermally evaporated and deposited onto the PMMA mask. The deposition rate and total thickness are monitored with a quartz crystal microbalance. A typical film thickness is a few 10 nm. The lateral size of the particles ranges from several 10 nm to a few μm . In arrays, the particles are arranged in square patterns with a typical distance in the order of 1 μm (for small particles).
2. In the lift-off step, the PMMA mask is dissolved in acetone, so that the excessive metal is detached from the substrate. The metal that has been deposited into the holes of the PMMA, i.e., directly onto the substrate, remains on the surface.

C. Positioning of colloidal nanoparticles

1. The colloidal nanoparticle solution is spin coated onto the PMMA mask.
2. The lift-off step dissolves the PMMA and removes the excess nanoparticles that have not been deposited in the mask holes. The particles directly on the substrate tend to stick to the surface.

In an optional step after the metal nanostructure fabrication or the positioning of nanoparticles, a protective layer of silicon dioxide (SiO_2) can be thermally evaporated to seal the fabricated structures. A typical layout of EBL fabricated structures is exemplary shown in Fig. 3.2 a). In the subfigures b)–d), single nanodisks of different sizes are shown. In the SEM³ image in b) the shape of the nanodisk can be seen, whereas in the TEM⁴ image c) the grain structure becomes apparent. Under oblique view in d) the edge profile of the nanodisks can be assessed and the surface roughness can be estimated to some extent.

3.1.2. Multiple step lithography

Complex nanostructures can be created by the combination of several successive lithography steps. In the context of this work, silver nanodisks with colloidal QDs deposited on defined positions are fabricated as sketched at

³scanning electron microscope

⁴transmission electron microscope

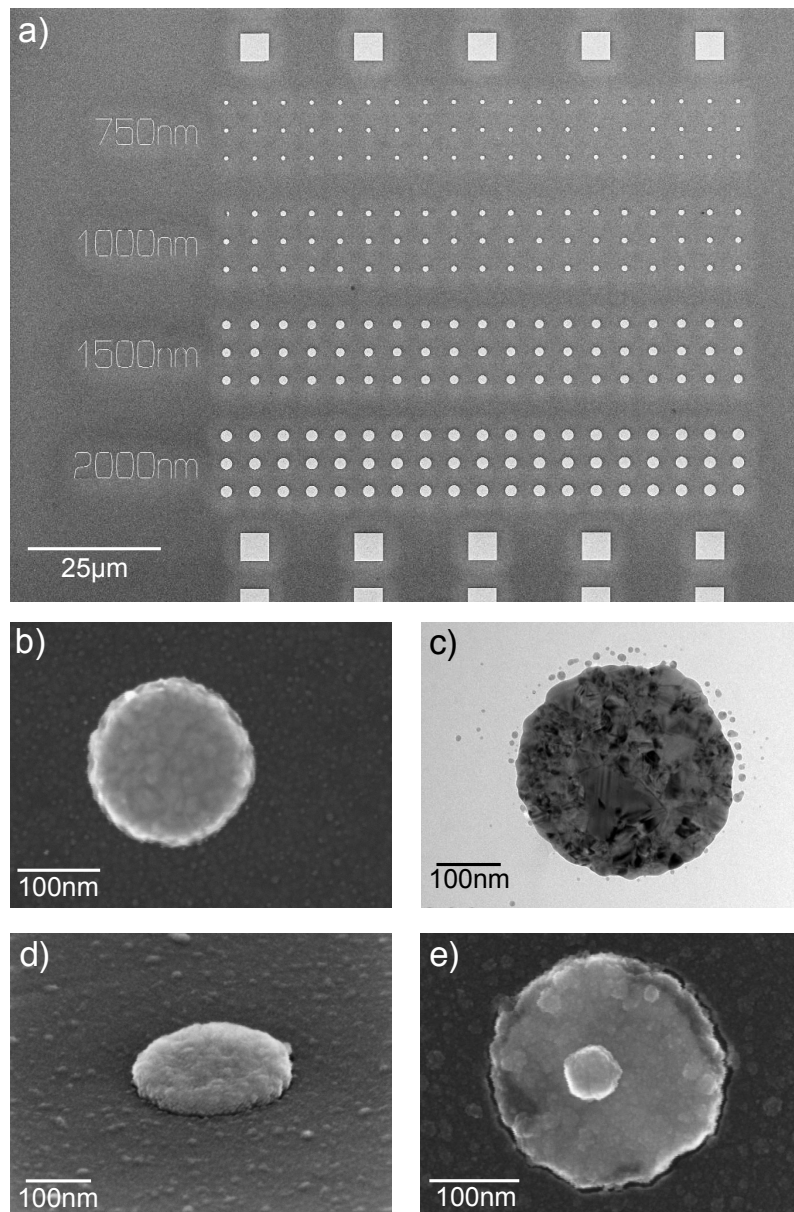


Figure 3.2.: Electron microscope images of EBL-fabricated silver nanostructures: a) Overview of a section with large disks 750–2000 nm in diameter and square structures with $5\ \mu\text{m}$ side lengths that serve as markers for optical microscopy. b) Nanodisk 200 nm in diameter, c) nanodisk 320 nm in diameter, d) nanodisk 220 nm in diameter under oblique view. d) Nanostructure built from QDs (60 nm diameter spot in the middle) and a silver nanodisk 315 nm in diameter, combined in a two-step EBL process. The images were acquired with a SEM except c) which is a TEM image.

the bottom of Fig. 3.1. An exemplary result can be seen in Fig. 3.2 e). To create such structures, the silver nanodisks are fabricated first, and the colloidal QDs are deposited onto the mask created by a subsequent lithography step. The experimental challenge is the alignment of the two structures, which is done by writing special position markers on defined positions in the first fabrication step. These markers are used to align the coordinate systems of the subsequent lithography steps. The achieved position accuracy is < 10 nm [27].

3.2. Spectroscopy of nanoparticle arrays

The optical characterization of EBL-fabricated nanoparticle arrays is carried out with *microspectroscopy*, combining an optical microscope⁵ with a spectrometer⁶. The use of a microscope enables to acquire spectroscopic data from a spatially confined area ranging from millimeters to a few hundred nanometers. The spectrometer is connected to the port of the microscope with an optical fiber. A halogen lamp is used as the light source, a polarizer and a tiltable sample holder enable to control incidence angle and polarization direction, respectively (Fig. 3.3).

Normalizing the light intensity transmitted through the nanoparticle array to the light intensity transmitted by the bare substrate, we can deduce what is absorbed or scattered by the nanoparticles. The size of the observation area depends on the diameter of the fiber core and the magnification of the objective. For a $10\times$ objective and the used fiber, the diameter of the measurement area is approximately $50\ \mu\text{m}$. The measured transmission spectrum of an array of nanoparticles is an average over $\approx 10^4$ particles.

Before the actual measurement, the fiber has to be aligned with the crosshair in the ocular. By doing so, it is possible to center the measurement area on the nanoparticle array. The next step is the determination of the correct exposure time, so that the whole dynamic range of the detector is used without overexposing the spectrum. To further increase the signal-to-noise ratio of the measurement, successive measurements can be averaged automatically. This is especially practical for transmission measurements in the blue spectral region, where the intensity of the used halogen light source is low. Averaging over 100 spectra results in measurement times in the range of a few 10 seconds.

⁵Zeiss Axioskop

⁶Zeiss MMS 1

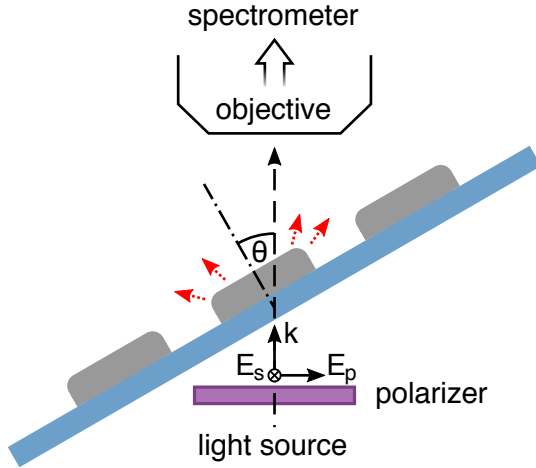


Figure 3.3.: Schematics of the optical characterization setup for nanoparticle arrays. A halogen lamp serves as light source and the transmitted light is analyzed in a spectrometer. The angle of incidence θ and the polarization direction (E_s, E_p) are adjustable.

When the correct exposure time has been determined, a so-called dark spectrum I_{dark} is taken. With the light source turned off, it is a measure of the dark current of the spectrometer diode array and the background noise. The dark spectrum I_{dark} represents an offset, that is subtracted from each transmission measurement I_{raw} to obtain the corrected transmission T :

$$T = I_{\text{raw}} - I_{\text{dark}}. \quad (3.1)$$

Subsequently, a transmission spectrum T_{ref} of the substrate (far from the nanoparticle array) is taken. This reference measurement allows the removal of the spectral dependence of the light source, the detector and the optical elements. The spectrum T of the nanoparticle array is divided by the reference spectrum T_{ref} to obtain the normalized transmission T_{norm} of the nanoparticle array,

$$T_{\text{norm}} = T/T_{\text{ref}}. \quad (3.2)$$

For the discussion we will use the extinction E , rather than the transmission. The extinction is the attenuation of light as a result of scattering S and absorption A :

$$E = S + A. \quad (3.3)$$

Incoming light of intensity 1 can either be transmitted, scattered or

absorbed, according to:

$$T + S + A = 1. \quad (3.4)$$

The extinction E is thus given by:

$$E = 1 - T_{\text{norm}} = 1 - T/T_{\text{ref}}. \quad (3.5)$$

For plasmonic structures, strong extinction occurs when light of a specific frequency is resonant with a plasmonic mode. This resonance leads to both, absorption and scattering, as discussed in the introduction in section 2.2.

3.2.1. Angle & polarization dependence

In the microspectroscopy setup, first we use a tiltable sample holder, which allows to change the angle of the incoming light relative to the substrate plane. Second, with a polarizer the direction of the electric field component of the incoming light can set to be parallel (p-polarized) or normal (s-polarized) to the plane of incidence, see Fig. 3.3.

3.2.2. Grating effects

Grating effects play a role when dealing with regular arrays (of EBL fabricated nanoparticles). The effect is governed by the grating equation (here, describing a transmission grating):

$$d_g(n_1 \sin \theta_1 + n_2 \sin \theta_2) = m\lambda, \quad (3.6)$$

where the subscript denotes the incident (1) or diffracted (2) light, $\theta_{1,2}$ are the angles relative to the grating normal and $n_{1,2}$ are the refractive indices on the respective sides of the grating (particle array). The letter m is the grating order, λ is the light wavelength and d_g is the grating constant, which equals the center-to-center particle distance. To facilitate the following explanation we consider normal incidence, $\theta_1 = 0$. Specific grating effects appear when the diffracted light corresponding to a grating order changes from evanescent to radiative character, i.e., $\theta_2 = 90^\circ$, and it has been shown that this condition plays a particularly important role for regular arrays of plasmonic nanoparticles [28]. This is the case for:

$$d_g = \frac{m\lambda}{n_{1,2}}. \quad (3.7)$$

Because diffraction can occur in forward and backward direction, n_2 becomes $n_{1,2}$, meaning that the condition is valid for n_1 (air) and n_2 (substrate). For a given value of d_g the wavelength range $\lambda > \frac{d_g n_{1,2}}{m}$ is thus radiative, while the range $\lambda < \frac{d_g n_{1,2}}{m}$ is evanescent, i.e, non-radiative. This leads to asymmetric spectra when a plasmon excitation peak spans an according wavelength range.

For incident light at an arbitrary angle θ_1 , the critical grating constant also depends on this angle, as shown in Eq. 3.6 (the condition for grazing angle is still $\theta_2 = 90^\circ$). For a constant angle of incidence θ_1 grating effects in a certain wavelength range can be avoided by adapting the design of the regular particle arrays accordingly. However, for varying angles of incidence θ_1 , grating effects have to be taken into account in the analysis of spectral data. A detailed study of the spectral features that arise from grating effects can be seen in Ref. [29].

3.2.3. Near-field coupling

Yet another effect of particle-particle interaction occurs if the interparticle distances are smaller than about the particle diameter. In this case, the particles can couple via their plasmonic near-fields. For example, for a particle dimer and polarization parallel to the long dimer axis this near-field interaction weakens the restoring forces in the single particles and leads to a redshift of the plasmon resonance [30]. To avoid near-field coupling and minimize grating effects, in this work, the interparticle distances of nanoparticle arrays is chosen as $1.2 \mu\text{m}$.

3.3. Single particle spectroscopy

For the spectroscopy of single particles a setup similar to the one described in the previous section is used. The main difference is that not transmitted light (of nanoparticle arrays) but scattered light from single nanoparticles is detected and analyzed. For that purpose, the setup incorporates dark field excitation, a piezoelectric stage⁷, a Czerny-Turner spectrometer⁸ and a highly sensitive camera⁹.

⁷Physik Instrumente GmbH, P517.3CL

⁸Andor, Shamrock SR-303i

⁹Andor, IXon DV885LC

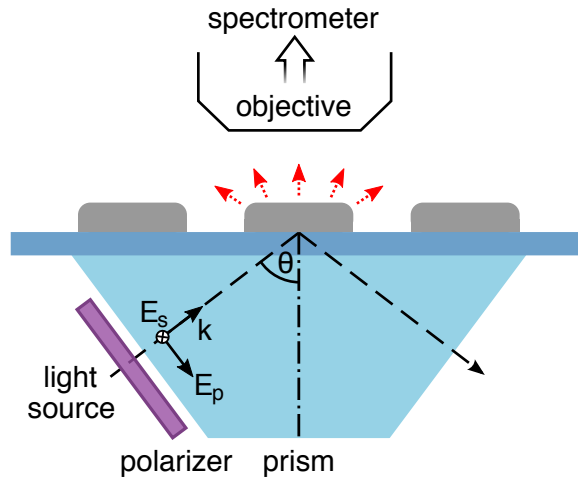


Figure 3.4.: Schematic of the single nanoparticle spectroscopy setup. The evanescent light of a white light (halogen lamp) beam that is totally internally reflected in a glass prism is scattered by single nanoparticles. The scattered light is collected by a microscope objective and analyzed in a spectrometer. The angle of incidence θ and the polarization direction (E_s, E_p) are adjustable.

3.3.1. Dark field excitation

Small optical signal intensities are advantageously detected in a dark field configuration, where the detection of the incident light is avoided and only scattered light (from individual nanoparticles) is detected. We use a total internal reflection geometry for sample illumination, as shown in Fig. 3.4. The sample is attached to a glass prism with immersion oil, so that the sample side of the substrate is facing away from the prism and towards the microscope objective. The excitation source is a halogen lamp, whose light is guided into the prism by a fiber bundle. The angle of incidence θ is large enough to ensure total internal reflection at the glass/air interface of the sample.

The evanescent field of the reflected light extends beyond the interface and can interact with the metallic nanoparticles on the surface. The light that is resonant with plasmonic structures is either absorbed or scattered. The unscattered (reflected) light exits the glass prism on the opposite side. Only the light that is scattered by the nanoparticles is collected by the microscope objective. This has the advantage that the background signal is low which results in a favorable signal-to-noise ratio.

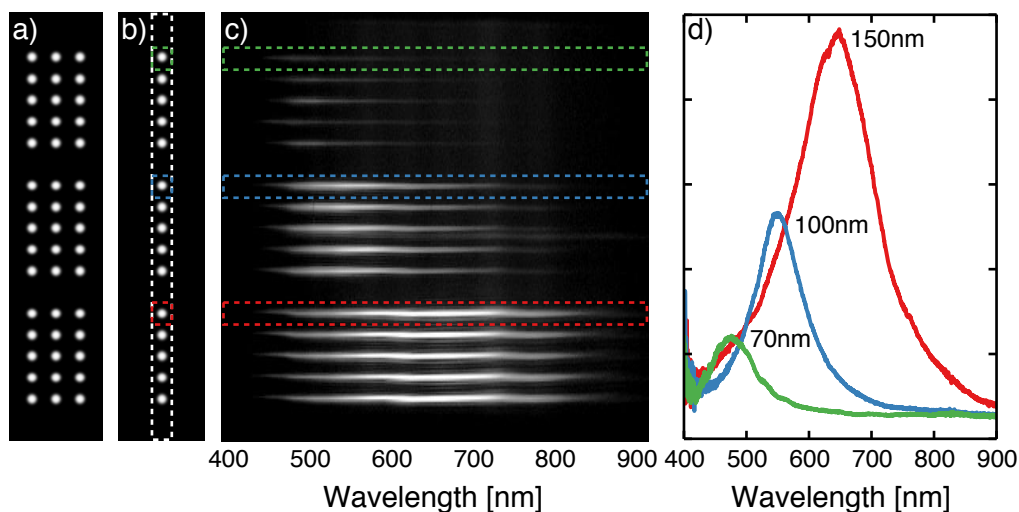


Figure 3.5.: Sample alignment for single particle spectroscopy based on a sample of silver nanodisks 70, 100 and 150 nm in diameter, indicated by the labels in d) and the colors. Sketches of the particle arrangement on the sample shown for a) open and b) closed slit for the diffraction grating reflecting the 0th order (mirror condition). c) Optical spectra, i.e., images of a higher grating order taken by the camera. d) The spectral information from c) can be extracted and plotted.

3.3.2. Single nanoparticle alignment

The scattered light is collected with a high numerical aperture (NA) objective (100 \times , NA = 0.95) and exits the microscope¹⁰ into the Czerny-Turner spectrometer whose slit (positioned in the image plane) can be adjusted in width from 10–2500 μm . For the 100 \times objective this translates to an rectangular measurement area ranging from a diffraction limited value to 25 μm in width.

By alignment of the sample with the slit, it is possible to spectrally analyze the scattered light from single nanoparticles. The procedure sketched in Fig. 3.5 makes use of turning motorized grating turret of the spectrometer. In a) the zeroth grating order is projected onto the camera, so that images of the sample can be taken. When the width of the slit is reduced in b), the opening can be aligned with one nanoparticle row by using the piezoelectric

¹⁰Nikon, Eclipse TE-2000-S

sample holder. After the alignment, the grating turret is turned, so that the a higher grating order is projected onto the camera. The resulting images are shown in c). The x-direction contains the spectral information (wavelength in nanometer) and the y-direction contains the spatial sample coordinate parallel to the slit. This means that multiple nanoparticles can be measured parallelly. The spectral data of individual nanoparticles in d) is obtained by summation over corresponding pixel lines and applying the normalization method explained in the following section.

3.3.3. Normalization of single particle scattering spectra

The camera features a 14 bit EMCCD (electron multiplying charge coupled device) type sensor. It has the ability to multiply charge on the sensor before readout, which makes it possible to record single photon events. The camera sensor is cooled to -70° to keep the thermal dark current of the CCD low. A low dark signal is crucial for low-light applications.

To quantify the dark signal of the sensor, images with closed shutter for several exposure times are taken and histograms of the pixel values of these images are plotted. These histogram are then fitted with a Gaussian function (see inset of Fig. 3.6 a)):

$$g(x) = a \cdot \exp\left(-\frac{1}{2} \left(\frac{x - c_{\text{off}}}{\sigma}\right)^2\right), \quad (3.8)$$

x is a certain pixel value, a is a constant, c_{off} is the offset from zero (corresponding to the average pixel offset) and σ is the standard deviation. It can be seen from Fig. 3.6 a) that the offset c_{off} is constant throughout a wide range of exposure times until 100 s, which is a particularity of the EMCCD sensor. To zero the counts, this offset is subtracted from each pixel value of the sensor. With the offset subtracted, the standard deviations of the Gaussian fits in Fig. 3.6 c) are a measure for the remaining random noise. Similarly to the time dependance of the offset c_{off} , the standard deviation σ is only weakly dependent on the exposure time. However, both, the offset and the noise level can depend on other measurement parameters, e.g., the electron multiplying gain.

In contrast to the dark signal of the EMCCD sensor, background signal intensities from, e.g., a non-perfectly adjusted dark field excitation setup are both exposure time and wavelength dependent. When necessary, spectra of the background I_{bg} are taken and subtracted from each dark field measurement.

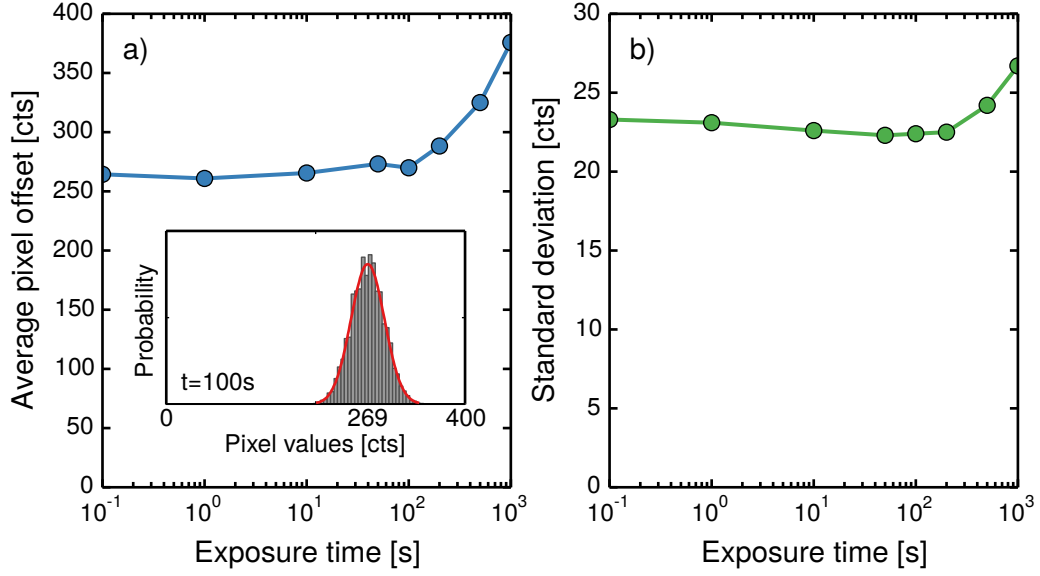


Figure 3.6.: Quantification of the dark signal of the EMCCD sensor for different exposure times. The distributions of the pixel values have been fitted with Gaussian functions, as shown exemplarily for $t = 100$ s in the inset of a). In a) the average pixel offset from the central position of the Gaussian and in b) the standard deviation of the pixel values from the width of the Gaussian are drawn. the latter is a measure for the random pixel noise.

For the measurement, not only the dark or background signal must be considered, but also the spectral dependency of the elements in the spectroscopy setup must be taken into account, e.g., the halogen light source, optical elements such as the fiber bundle, lenses and the spectrometer grating. In addition, the EMCCD sensor has a varying quantum efficiency dependent on photon energies. This means that a reference spectrum I_{ref} is essential to obtain meaningful spectral information. The correct reference is a spectrum of the excitation light, i.e., the halogen lamp. The corrected single particle scattering intensity S is then calculated by:

$$S = \frac{I_{\text{raw}} - I_{\text{bg}}}{I_{\text{ref}} - c_{\text{off}}}. \quad (3.9)$$

I_{raw} is the uncorrected scattering spectrum, I_{bg} is the background intensity and c_{off} is the average dark signal (offset) of the sensor.

3.4. Fluorescence spectroscopy

The setup for the fluorescence spectroscopy is integrated into the same microscope as the single particle scattering setup. Whereas in the previous setup the light from a halogen lamp is scattered by nanoparticles, the goal of fluorescence spectroscopy is to study the light emission of fluorophores.

Fluorescence is a process where an emitter is brought into an excited electronic state by absorption of a photon from the excitation light source. The excited emitter relaxes to the ground state and emits a photon. In most cases the emission light has a lower energy than the excitation light. For the practical realization this means that a special filter set with a dichroic mirror can be used to separate excitation and emission light. A schematic of the fluorescence spectroscopy principle is drawn in Fig. 3.7. The dichroic mirror¹¹ is reflective for the excitation (laser) light, but the longer wavelength fluorescence emission passes through. This means that the excitation light is blocked from the optical path and only the fluorescence emission is analyzed in the spectrometer. In addition, an excitation filter¹² is used to select the excitation wavelength of the light from the light source, and an emission filter¹³ only transmits the fluorescence light, i.e., further blocks the excitation light.

For the fluorescence spectroscopy of QDs with a center emission wavelength of 535 nm, a diode laser¹⁴ with emission wavelength of a 375 nm is used as the light source. The output is a collimated beam with elliptical cross section, shaped into circular form by a pinhole before it is guided into the microscope and passes the excitation filter. As for the actual measurement a defocused laser spot is desirable, a biconvex lens with 30 cm focal length is inserted at the microscope entrance port ≈ 15 cm from the objective. This results in a homogeneously illuminated area on the sample plane.

As a sidenote, this excitation configuration can be easily combined with the prism coupling excitation for nanoparticle scattering from the previous section. In addition, both, the fluorescence light from emitters and the scattered light from the nanoparticles, can pass the dichroic mirror and the emission filter and can be analyzed with the spectrometer. This means that both measurements can be done in an alternating manner on the same sample position by switching the respective light sources on and off.

¹¹Semrock, HC BS 409

¹²Semrock, BrightLine HC 370/36

¹³Semrock, Edge Basic 405 LP

¹⁴Becker and Hickel BDL-375

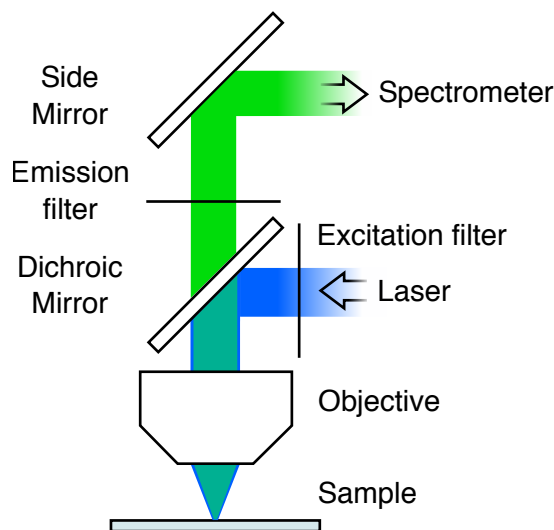


Figure 3.7.: Schematic of the fluorescence spectroscopy setup. Light from a laser source passes through the excitation filter and excites fluorophores on the sample. The fluorophore emission passes the dichroic mirror and the emission filter and is subsequently analyzed in a spectrometer. The filters are matched in a way that the excitation light is reflected by the dichroic mirror and also cannot pass the emission filter.

3.4.1. Normalization of fluorescence spectra

Generally speaking, spectroscopy methods can be calibrated very accurately wavelength-wise, but measuring spectral intensities quantitatively is much more difficult to accomplish due to the wavelength dependency of the measurement setup itself. While for transmission and scattering measurements, by normalization with the respective light sources, the wavelength dependency cancels out, this is not possible for fluorescence spectroscopy because there is an energy conversion through absorption and re-emission.

To measure correct (relative) intensities, the integral spectral dependence of the fluorescence spectroscopy system must be determined. For this purpose, the light from a calibrated light source¹⁵ is measured and subsequently normalized by the spectral data supplied by the manufacturer to obtain the integral spectral dependence of the setup. This can then be used to normal-

¹⁵Avantes, AvaLight-HAL-CAL

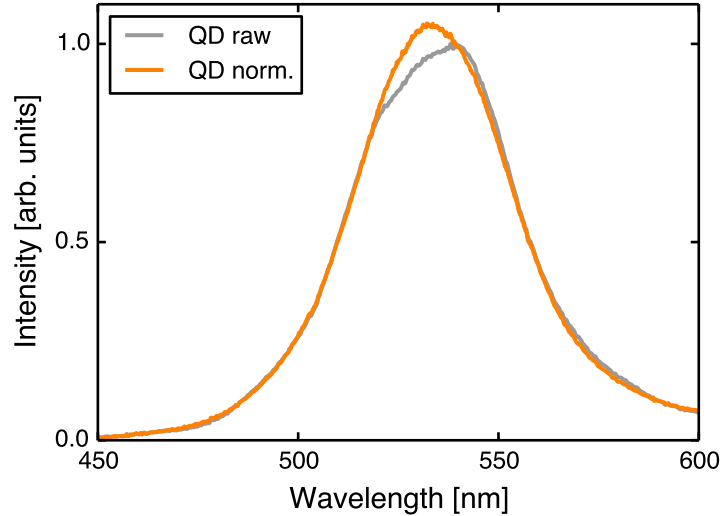


Figure 3.8.: Fluorescence spectra of QDs (obtained by summation of 35 individual QD ensembles 50–100 nm in diameter on quartz substrate), that show the effectiveness of normalization. The raw untreated spectrum (grey) shows artefacts from the spectral dependence of the setup, the normalized spectrum (orange) is smooth.

ize measured fluorescence spectra. The importance of this procedure can be seen in Fig. 3.8, where the raw and the normalized emission spectrum of QDs are compared. The normalized spectrum is smooth as one would expect for an inhomogeneously broadened emission of many QDs (orange curve in Fig. 3.8). The raw spectral signature (grey curve) is significantly distorted around the peak position due to the spectral dependencies of the setup.

3.5. Time correlated single photon counting

In the time correlated photon counting (TCSPC) technique, fluorophores are excited by a short laser pulse, and the photon arrival times are recorded by an avalanche photo diode¹⁶ and a TCSPC electronics module¹⁷. From

¹⁶PicoQuant, τ -SPAD-50

¹⁷Becker & Hickl, SPC-830

the time dynamics the mean lifetime of the fluorophores can be calculated. For a review of time correlated photon counting techniques see Ref. [31].

3.5.1. Measurement setup

Figure 3.9 shows a schematic of the TCSPC setup built into an optical microscope, identical to the one used for the single particle scattering setup. Light from a pulsed laser diode¹⁸ with an emission wavelength of 483 nm and a pulse duration of 60–90 ps (full width at half maximum) passes a beam shaper (a pinhole placed between two lenses), an optional lens for defocused illumination, a filter set for fluorescence detection and is then directed onto the sample by the microscope objective (100 \times , N = 0.95). The emission from the excited fluorophores on the sample is collected by the microscope objective and subsequently passes a pinhole (75 μ m in diameter) that is positioned in the focal plane. The pinhole reduces the size of the measurement spot on the sample to a small area of 750 nm in diameter. The light that passes the pinhole is focussed onto an avalanche photodetector (APD) that is connected to the TCSPC module.

The TCSPC module is a multichannel analyzer that features an analog-to-digital converter with 12 bit time resolution. For a typical measurement window of 100 ns this results in a time resolution of 100 ns/4096 = 24 ps. For the lifetime measurement, the time between the laser trigger signal and the detection signal from the avalanche photodetector is recorded by the TCSPC module. This process is repeated with the laser repetition rate of several MHz. The total measurement time is typically several minutes.

3.5.2. Fluorescence lifetime analysis

The fluorescence lifetime τ is the average time that a fluorophore stays in its excited state, before decaying radiatively into its ground state by emitting a photon. A population of excited fluorophores follows an exponential decay, i.e, after the fluorescence lifetime τ the number of excited fluorophores is reduced by a factor of e . For the simplest case that only one (radiative) decay channel with a certain lifetime exists, the emitted fluorescence intensity I is described by a mono-exponential function:

$$I = I_0 \exp(-t/\tau). \quad (3.10)$$

¹⁸PicoQuant, PDL-800-D laser driver, 1013440 laser head

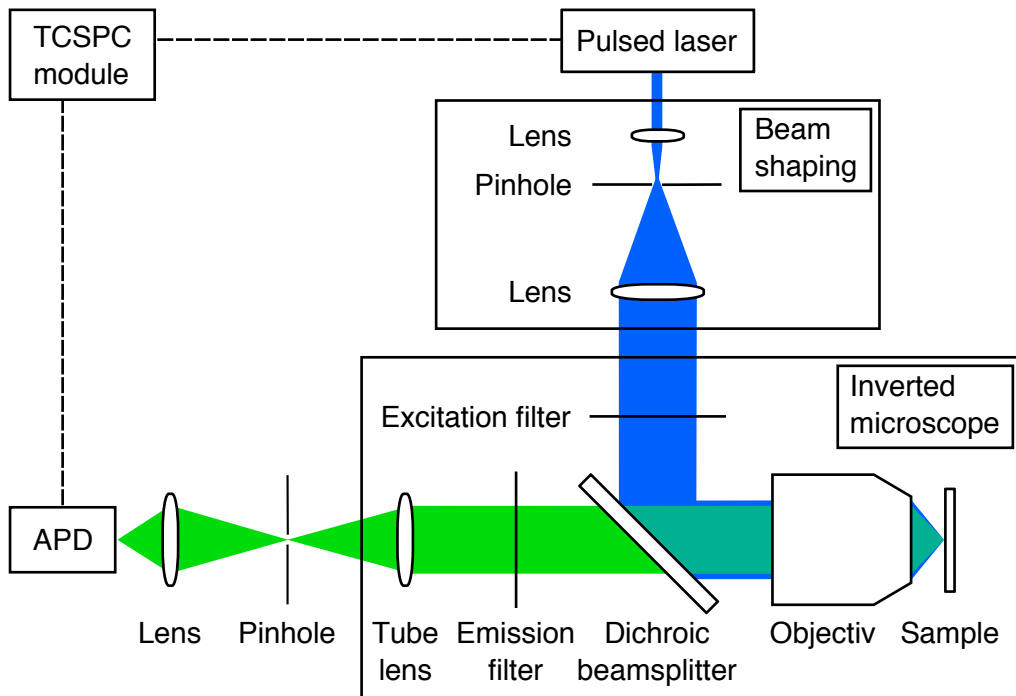


Figure 3.9.: Schematic of the TCSPC setup. Fluorophores on the sample are excited by a pulsed laser and the photon events of the emission are measured by an avalanche photo diode (APD). The TCSPC module calculates the photon arrival times from the laser trigger signal and the avalanche photo diode signal. Adapted from [27].

The fluorescence lifetime τ is inversely proportional to the decay rate $\Gamma = 1/\tau$ of the relaxation process.

In the TCSPC measurement, photon arrival times are recorded. A histogram of these arrival times shows the time dependence of the fluorescence intensity. For a single exponential decay, the fluorescence intensity decreases linearly in a semi-logarithmic plot and the lifetime can be extracted from its slope, or by a fit with Eq. 3.10.

In practice, there can be different radiative and non-radiative decay channels with different lifetimes. It may be necessary to fit the fluorescence time traces with a multi-exponential function to assess the different lifetimes, however, separation is only possible for distinct lifetimes. Especially for emitters in the vicinity of plasmonic nanostructures, (section 2.5) a continuous distribution of lifetimes exists that is challenging to describe. This is further discussed in section 5.3.

3.6. Numerical simulation of plasmonic nanoparticles

The numerical simulations in this work are done using the metal nanoparticle boundary element method (MNPBEM) toolkit¹⁹. It was developed by U. Hohenester and A. Trügler [12] and is based on a boundary element method approach [32] [33]. The toolkit is implemented in the MATLAB® programming language and solves Maxwell's equations for homogeneous dielectric functions, that are separated by abrupt interfaces.

Boundary element methods are a class of discrete numerical methods for the calculation of linear partial differential equations for certain boundary conditions. Only the discretized interfaces (surfaces) are used for the calculation, which is more favorable in terms of computational effort than a complete volume discretization in finite-difference time-domain (FDTD) [34] or discrete dipole approximation (DDA) [35] methods.

BEM approaches rely on linear homogeneous media, i.e., dielectric functions, this is less general than the above mentioned methods. However, this simplification is well suited for the simulation of metallic nanoparticles in dielectric media [12]. The BEM method for solving Maxwell's equations uses effective charges and currents for discrete points (in the middle of the respective discretized surface elements) to solve the boundary conditions for an incident oscillating field. After a self-consistent calculation of surface charges and currents (matrix inversion), the resulting fields can be calculated with a Green's-function approach.

A key feature of the MNPBEM toolkit is the implementation of modular MATLAB classes, that can be combined to cover a variety of applications. Figure 3.10 gives an overview of the basic elements of a MNPBEM simulation. The first step is to discretize the particle boundaries. The obtained discrete mesh is combined with the respective dielectric functions. Depending on the application, the plasmon excitation can be simulated by impinging electron beam (EELS), plane wave illumination (optical measurements) or an oscillating dipole. Since, there are different BEM solvers for each excitation method, it has to be decided whether a quasi-static approximation is sufficient or retardation should be taken into account. The solver is subsequently used to calculate the surface charges at the discretized boundaries. From these surface charge maps, the desired measurement quantities, such as energy loss spectra or scattering and absorption cross sections are calculated. More information can be found in the user guide²⁰ and in Ref. [36].

¹⁹Version 11

²⁰Available at <http://physik.uni-graz.at/~uxh/mnpbem/mnpbem.html>

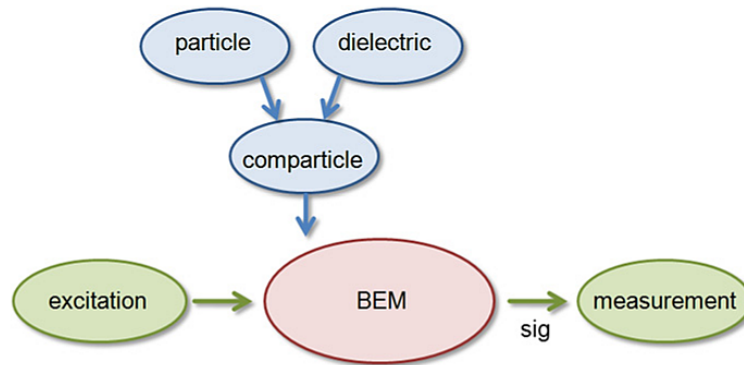


Figure 3.10.: Flowchart of the basic elements of a nanoparticle simulation with the MNPBEM toolbox. From Ref. [12].

3.6.1. Surface discretization

For the discretization of the particle boundaries, the MNPBEM toolkit relies on the MESH2D program²¹, which provides triangulation routines that facilitate the generation of two-dimensional meshes.

To create numerical representations of EBL fabricated particles, the `polygon` class can be used to create the outline of the particles which can then be subsequently meshed and extruded to create a three dimensional model. This approach is explained in the MNPBEM user guide. The necessary steps for the modelling of a disk are illustrated in Fig. 3.11 and discussed in the following.

The first step, shown in a) is the creation of the particle outline: the outline of a disk is a circle, approximated by a regular polygon. In b) the area of the circle is filled with triangular surface elements. The important parameter for this triangulation procedure is the maximum allowed element size (in nm) `hmax` which is used to control the density of surface elements. In c) the lateral surface of the disk is created by extruding the circle to the height of the disk. In this step the particle edges are rounded off, and as a side effect, the resulting lateral size of the particle becomes (≈ 10 nm) larger than the size of the initial polygon. To account for this difference, the lateral expansion of the disk is scaled to the correct size.

The simulations in this work are done for nanodisks 115–315 nm in diameter and 30 nm in height. The respective discretized nanodisks are built from regular polygons with 96 edges, with a maximum surface element size `hmax`

²¹By Darren Engwirda, available from <http://www.mathworks.com>

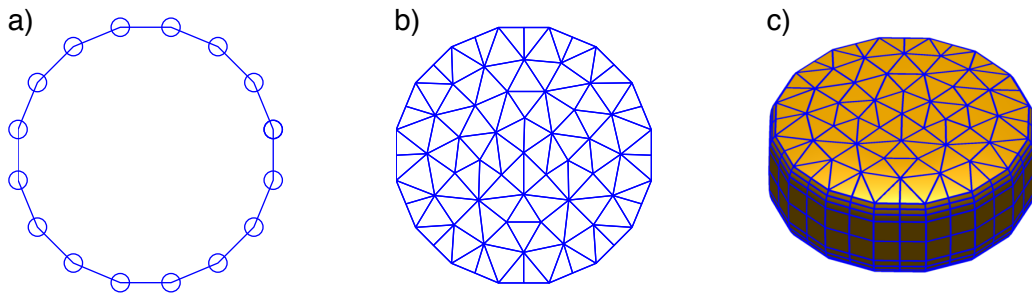


Figure 3.11.: Discretization of a nanodisk 75 nm in diameter and 30 nm in height. a) The outline of the disk is a regular polygon. b) The surface of the polygon is meshed using the MESH2D program. c) For the final shape the outline is extruded in the third dimension and the bottom surface is added. The number of surface elements in this simple model is 464.

of 10 nm. For these parameters, the simulations²² converge, i.e., simulations with a finer discretization yield the same results. Calculation times for the above nanodisk diameters range from roughly 30 min to 2 h for one spectrum with 100 sampling points, i.e., wavelengths when the code is run on a current desktop computer²³. Convergence is shown in Fig. 3.12 for simulated extinction spectra considering plane wave excitation of a) nanodisks 215 nm in diameter and b) nanodisks with 315 nm in diameter with different discretization parameter **hmax**. The spectra for a maximum element size **hmax** of 10 nm are identical to the spectra for **hmax** of 7 nm, even though the number of elements is 72 % higher for the nanodisk 215 nm in diameter or 50 % higher for the nanodisk 315 nm in diameter, respectively.

²²with retarded BEM solver: `bemret(p, [], green.options('cutoff', 5))`

²³Intel i7-920, 2.7 GHz quad-core CPU

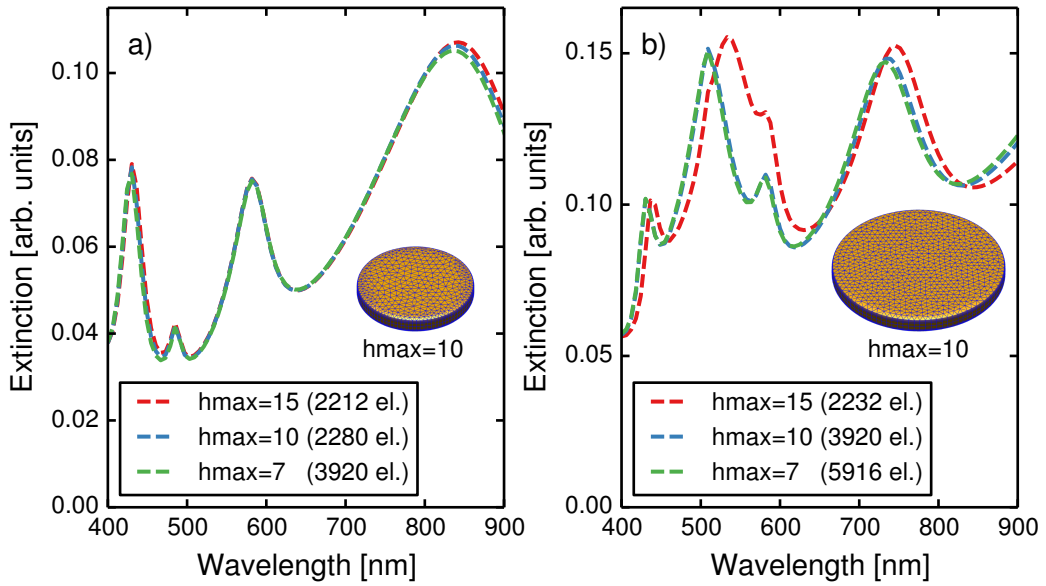


Figure 3.12.: Simulated extinction spectra (upon perpendicular incidence of a plane wave, retardation included) of nanodisks a) 215 nm and b) 315 nm in diameter and 30 nm high for different maximum allowed surface element size h_{\max} (in nm). The total number of surface elements is shown in parentheses. The insets show the discretized nanodisks for h_{\max} of 10 nm.

4. The mode spectrum of plasmonic nanodisks

In this chapter, the results of a spectroscopic investigation of silver nanodisks with accompanying numerical simulations are presented. Beforehand, we discuss a study of the plasmonic properties of silver nanodisks with electron energy loss spectroscopy (EELS) by Schmidt et al. [5], where a new mode family – the breathing modes – has been discovered. This result provides the starting point for this work.

4.1. Electron energy loss spectroscopy of nanodisks

To discuss the results of electron energy loss measurements of silver nanodisks by Schmidt et al. [5], the used EELS technique is first introduced briefly. It is deployed in a scanning transmission electron microscope (STEM), where a narrow monochromated electron beam is scanned over the sample. The applicability of the EELS technique for plasmonics benefits from the fact that an electron beam loses energy to plasmonic excitations when passing by or through a metallic nanostructure. Electrons induce collective excitations of the conduction electrons in the nanostructure, i.e., plasmons, which retroact on the electron beam. This results in a kinetic energy loss of the passing electrons that is specific to an excited plasmon mode and can be subsequently measured in an electron spectrometer.

Because of the high spatial resolution in a STEM, detailed plasmonic maps can be created by arranging the position resolved electron energy losses into 3-dimensional datacubes as sketched in Fig. 4.1. The x and y coordinates correspond to the lateral positions on the nanoparticle and the z coordinate is the energy resolved electron loss. That means that for a certain energy slice ΔE we obtain a 2-dimensional plasmonic map of a metallic nanostructure.

Concerning the physical interpretation of the obtained EELS data in the context of plasmonic nanostructures, it has been suggested that electron energy loss density is directly related to the photonic local density of states (LDOS) [37] of plasmonic nanostructures. This quantity is a measure for

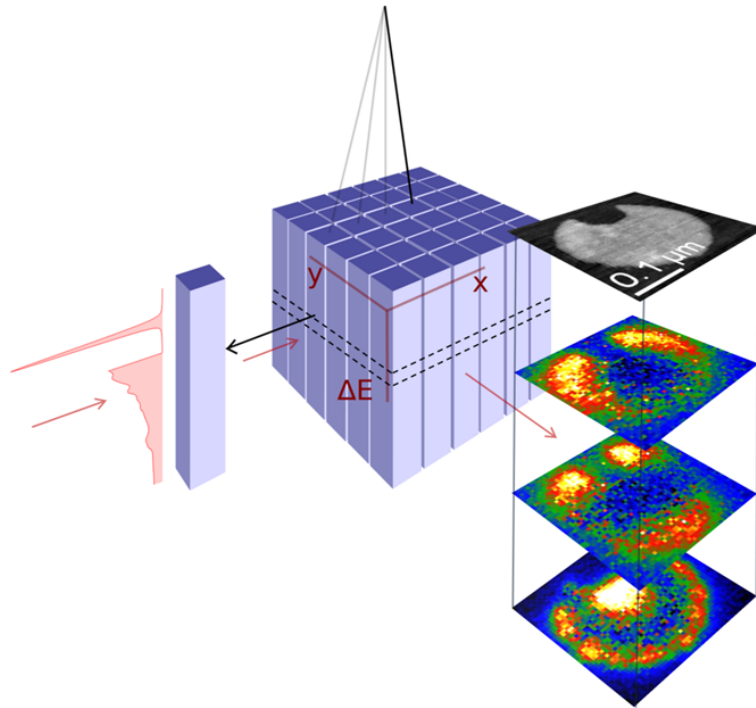


Figure 4.1.: Visualization of the 3-dimensional datacube obtained by electron energy loss spectroscopy (EELS). Lateral positions on the nanoparticle are in the (x,y) -plane, electron energy losses are plotted in the z -direction.¹

the number of electromagnetic modes that can be occupied by photons at a certain position in space. However, it has also been pointed out that even though the agreement of LDOS and EELS rate is quite good, a direct relation between EELS rate and LDOS cannot be given [38]. In addition, the electron beam interacts directly with plasmonic modes, i.e., with components parallel to its trajectory (z -direction). That means that plasmonic excitations with no or weak z -components are invisible in EELS.

The effect of the fast electrons passing by the structure of interest can be interpreted as an electromagnetic excitation short in time but broad in frequency. Therefore, the electrons can excite plasmonic modes with a multitude of resonance frequencies. There is no restriction to those plasmonic modes that possess a dipole moment as with optical methods.

In the theoretical introduction in section 2.2, the fundamental particle

¹Courtesy of F.-P. Schmidt.

plasmon has been introduced as a dipolar charge oscillation. Its dipolar character enables the resonant coupling to the electric field of an electromagnetic plane wave, which is a property of optically *bright* modes. In addition to this dipolar mode, it has been mentioned that a variety of further plasmonic modes exists, which do not necessarily have a net-dipole moment, and can thus be optically *dark*.

Nevertheless, these *dark* plasmonic modes can be accessed via EELS [39]. The results of an EELS characterization of a silver nanodisk 200 nm in diameter and 30 nm in height are shown in Fig. 4.2. Column a) shows EELS spectra acquired from specific areas on the nanodisk (blue) and the accordingly calculated spectra (red). In addition, measured b) and simulated c) EELS maps for specific plasmon modes are shown. On the very right side, the according surface charge maps are shown. From the surface charges, the mode labeled (A) can be identified as the familiar *dipolar* excitation, whereas modes (B) and (C) depict the multipolar *quadrupole* and *hexapole* modes, respectively. The map in (D), however, belongs to a previously undiscovered plasmonic mode family. Here, conduction electrons oscillate simultaneously towards the middle, resulting in radial symmetric surface charge variations. In analogy to radial acoustic modes on membranes, the mode is thus termed *breathing* mode [5]. What is specific about this mode is that it is a dark mode and that from all the nanodisk modes it couples strongest to the electron beam, due to strong field components parallel to the electron beam. The remaining EEL map in (E) is a *double breathing* mode, a hybrid mode between the dipolar and the breathing mode. The central aim of this work is to find a way to probe these breathing modes optically.

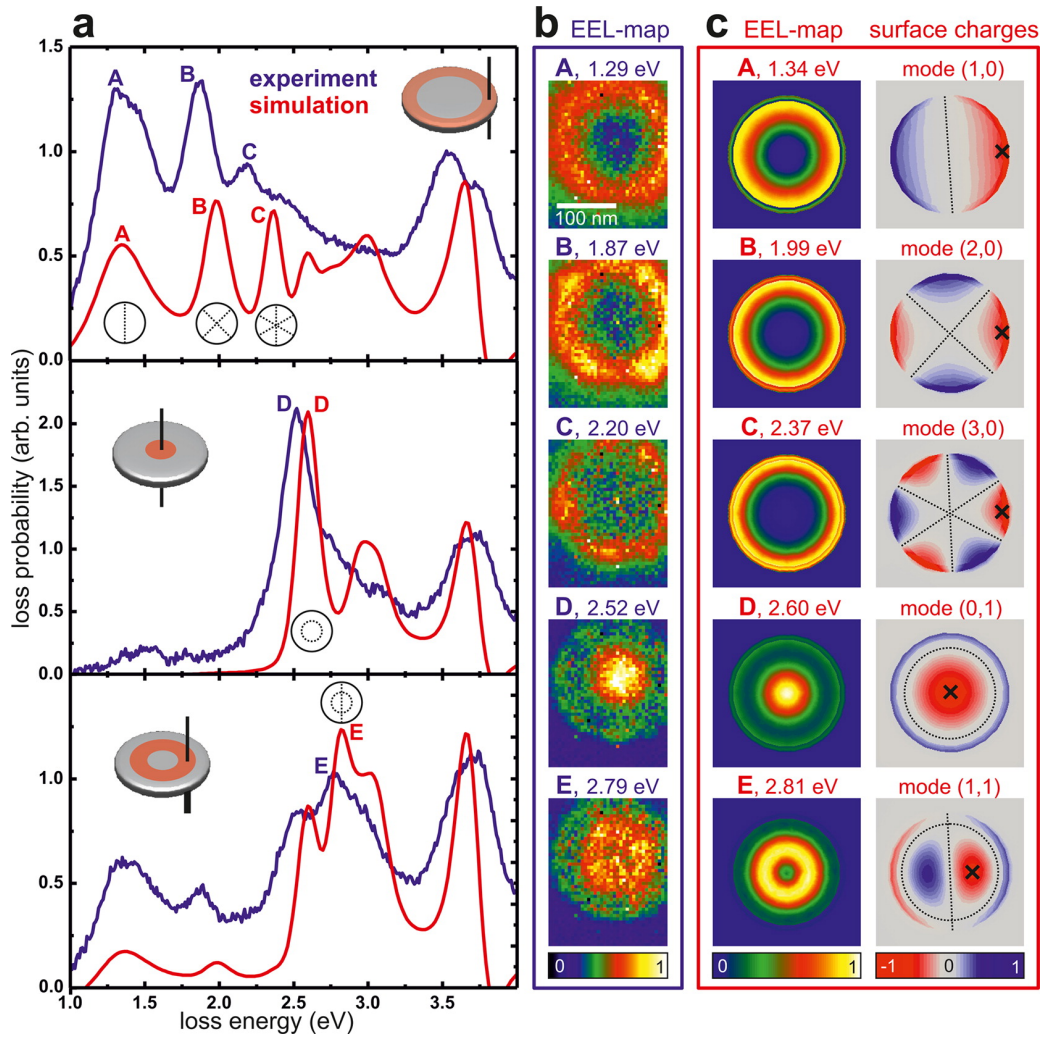


Figure 4.2.: EELS measurements of the plasmonic mode spectrum of a silver nanodisk 200 nm in diameter and 30 nm in height on a 30 nm thick Si_3N_4 substrate. a) Measured (blue) and simulated (red) spectra from the nanodisk regions indicated in the insets, b) measured and c) simulated EELS maps and surface charge maps. From Ref. [5].

4.2. Optical spectroscopy of nanodisk arrays

We start the optical measurements with a spectroscopic study on EBL fabricated nanodisk arrays that allow straightforward transmission microspectroscopy due to the large number of involved identical particles (several 10^3), leading to a good signal-to-noise ratio. The fabricated arrays consist of nanodisks 115–315 nm in diameter, with an array constant d_g of $1.2 \mu\text{m}$. SEM images of these nanodisks are shown in Fig. 4.3 a) and Fig. 3.2. The optical transmission data of the nanodisk arrays are plotted in terms of optical extinction which is $1 - \text{transmission}$ (see Eq. 3.5).

For the interpretation of the acquired spectra, we perform simulations with the MNPBEM toolkit [12], which has been introduced in section 3.6. With these simulations, Maxwell's equations are solved numerically for the discretized nanodisks, e.g., for the nanodisk 115 nm in diameter shown in b). Matching the measurement, a plane wave excitation with incident angle θ and polarization (E_s, E_p) is used. Because the nanodisk diameters are comparable to the wavelength, a BEM solver for the complete Maxwell equations is employed, taking into account field retardation.

Figure 4.4 depicts a direct comparison of an extinction measurement of nanodisks 115 nm in diameter with the corresponding simulations. In the simulation, the presence of the glass substrate is included by an effective dielectric function n_{eff} , as discussed in the following section. In the simulation, plasmonic modes can be identified by calculating the surface charges of the nanodisks at the center wavelengths of extinction peaks. These surface charges are described by complex numbers due to the displacement amplitude of the electrons and their phase relation to the driving field.

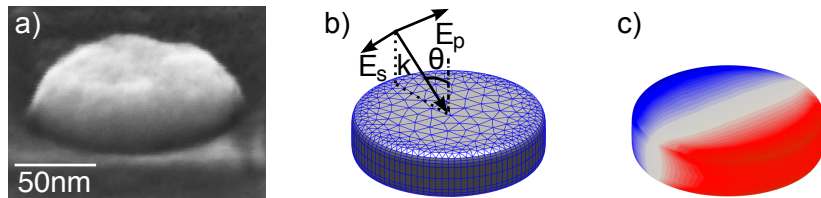


Figure 4.3.: Silver nanodisk 115 nm in diameter and 30 nm in height: a) SEM image under inclined view, b) numerical representation with discretized surface elements (θ incidence angle, \mathbf{k} wave vector, E_s, E_p electric field vector for s- and p-polarization, respectively) and c) surface charge map of the plasmonic dipole mode at 560 nm resonance wavelength (compare Fig. 4.4).

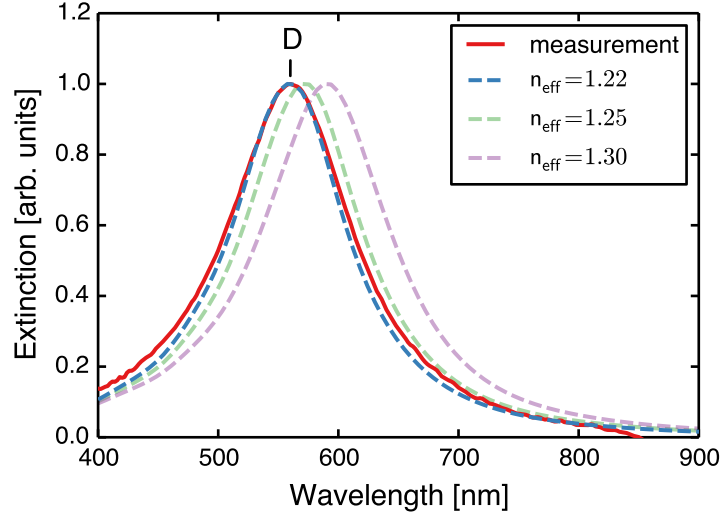


Figure 4.4.: Extinction spectra of silver nanodisks 115 nm in diameter and 30 nm in height at normal incidence. The peak corresponds to the plasmonic dipole excitation (D) (see Fig. 4.3 c)). The measurement is compared with BEM simulations for several effective refractive indices: $n_{\text{eff}} = 1.22$ is the best fit to the experiment, $n_{\text{eff}} = 1.25$ is the average of the dielectric functions of the substrate and air and $n_{\text{eff}} = 1.30$ is the effective refractive index, that describes best the positions of the quadrupole mode (see Fig. 4.5).

The real and imaginary parts of the calculated surface charges are equivalent in the way that the mode structure can be seen from both, however, the real part vanishes exactly at resonance. Therefore, the imaginary part of the surface charges is more suited for the determination of the modes – it is used throughout if not otherwise mentioned. The imaginary part is a measure for the losses of the system and it is maximum at resonance. Figure 4.3 c) depicts a map of the imaginary part of the surface charges at the resonance wavelength (see Fig. 4.4, blue dashed curve). From the dipolar character of the surface charge distribution we deduce that the dipole mode (D) is observed.

For normal incidence in the above mentioned case, the phase of the incoming plane wave is constant across the particle at a given time. For inclined incidence, phase retardation becomes important and, as a consequence, the

phase of certain modes can differ by $\pi/2$ from the dipole mode. Because of this difference in phase, their mode structure at the resonance can be seen from the real part of the complex surface charges. This particularity arises from the definition of the phase relative to the center of the coordinate system in the simulation.

4.2.1. Adaption of the numerical simulation to the measurement

SEM measurements of the EBL fabricated nanodisks are discussed in section A.2.1. The nanodisk diameters are 15 ± 7 nm larger than the nominal diameters (100–300 nm) for the EBL fabrication. Consequently, these nanodisk diameters (115–315 nm) are used in the simulation.

The simulation results are extinction cross sections C_{ext} (in nm^2). To facilitate the direct comparison with the nanoparticle array measurements, the simulated cross sections are converted into extinctions E of particle arrays by dividing the extinction cross section C_{ext} of a single nanodisk by its respective area d_g^2 in the array, taking into account the angle of incidence θ :

$$E = \frac{C_{\text{ext}}(\theta)}{d_g^2 \cos \theta}. \quad (4.1)$$

It turns out that for most cases the relative height of the extinction peaks in the experiments is smaller than for the simulations, although no obvious reason is apparent. Apart from this small deviations in the peak height, the agreement of simulation and experiment is excellent throughout.

We note that while a fixed angle of incidence is assumed in the simulations, a range of angles is present in the measurement. For the used objective ($10\times$, $\text{NA} = 0.25$) the half opening angle is 14.5° . In practice, the effect of this angular distribution is negligible, at most, it affects the comparison of relative intensities from simulation and measurement. The simulations are calculated for one polarization direction. To match the unpolarized measurements, the arithmetic mean of s- and p-polarized simulated spectra is taken, by adding the spectra and dividing by a factor of two.

The MNPBEM calculations are restricted to metallic nanoparticles in a homogeneous medium, i.e., a substrate could not be considered. Therefore, an *effective* dielectric constant ε_{eff} of the homogeneous medium surrounding the particle is used. In terms of refractive indices ($\varepsilon_{\text{eff}} = n_{\text{eff}}^2$), the effective refractive index can be approximated from an average of the dielectric constant

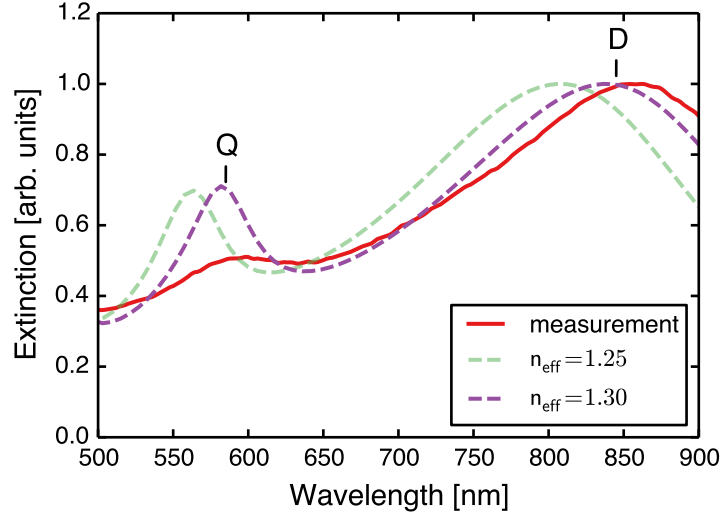


Figure 4.5.: Extinction spectra of nanodisks 215 nm in diameter and 30 nm in height at an oblique incident angle $\theta = 45^\circ$. The measurement is compared to BEM simulations assuming $n_{\text{eff}} = 1.25$ and $n_{\text{eff}} = 1.30$. The latter fits best to the positions of the quadrupole mode (Q). The dipole mode peak (D) is visible as well.

of the substrate n_{sub}^2 and the surrounding medium, i.e., air ($n_{\text{air}} = 1$) [40]:

$$n_{\text{eff}}^2 = \frac{1}{2}(1 + n_{\text{sub}}^2). \quad (4.2)$$

From this formula an effective refractive index for fused quartz substrates ($n_{\text{sub}} = 1.46$) of $n_{\text{eff}} = 1.25$ is obtained. However, this value can only be an approximation because the influence of the substrate depends on the geometry of the nanostructures and the field distribution of the plasmonic mode, i.e., its near-field pattern. Therefore, it has been suggested that the effective refractive index is taken as a fit parameter of the experiment [41].

In Fig. 4.4, the measured extinction for nanodisks 115 nm in diameter is compared with simulations for several refractive indices. While the simulation $n_{\text{eff}} = 1.25$ is in good accordance with the measurement, a fit yields an optimum value of $n_{\text{eff}} = 1.22$.

In the following, we are concerned with higher order modes of nanodisks. From the comparison of measurement and simulation with different refrac-

tive indices, we find that the influence of the substrate on higher order modes tends to be stronger, which results in a blue shift of the measured spectra compared to the simulated data with $n_{\text{eff}} = 1.25$. To account for this shift, a refractive index of $n_{\text{eff}} = 1.30$ is used throughout this chapter. An example relying on a comparison of simulation and experiment for nanodisks 215 nm in diameter and 30 nm in height at oblique angle of incidence is shown in Fig. 4.5. The effective refractive index is fitted to the quadrupole mode (Q), showing best agreement for $n_{\text{eff}} = 1.30$. For the dielectric function of silver, literature values by Johnson and Christy [42] are used.

4.2.2. Changing nanodisk diameter

Figure 4.6 a) shows a compilation of extinction spectra of nanodisks from 115 nm to 315 nm in diameter, as indicated at the right-hand side of b), and a height of 30 nm on quartz substrate. The measurement is done at normal incidence $\theta = 0^\circ$ and unpolarized illumination. The smallest nanodisks (115 nm in diameter) have already been discussed in the introduction (Fig. 4.4), the peak at 560 nm corresponds to the dipolar mode. For increasing particle diameter (while keeping the particle height constant) we observe a shift of the dipole peak to longer wavelengths. This behavior is typical for plasmonic nanoparticles and allows the tuning of the resonance throughout the visible and near-infrared spectral range. This effect is not directly related to the absolute size of the particles, but in fact is a matter of *aspect ratio*, i.e., the ratio of particle diameter and height. Due to the fabrication process, the height of the nanodisks is constant on a given sample. However, the particle diameter, and thus the aspect, can be varied lithographically. This point is illustrated schematically in Fig. 4.7 a).

The effect of aspect ratio on the resonance wavelength can be explained intuitively. With increasing aspect ratio the charges that accumulate on opposite sides of the particle are less or further apart – depending on whether the particle is flattened or stretched – and so the restoring force due to *Coulomb attraction* is weaker. Thus, the resonance frequency is smaller and the resonance wavelength is red-shifted.

The same insight can be obtained by regarding nanodisks as flatted spheres, as illustrated in Fig. 4.7 b). Flattened spheres are so-called *oblate ellipsoids* and their plasmon modes can be described analytically, see, e.g., Ref. [18]. In brief, the resonance condition is given in terms of the dielectric function $\varepsilon(\omega)$:

$$\text{Re}[\varepsilon(\omega)] = \varepsilon_m \left(1 - \frac{1}{L_j}\right), \quad (4.3)$$

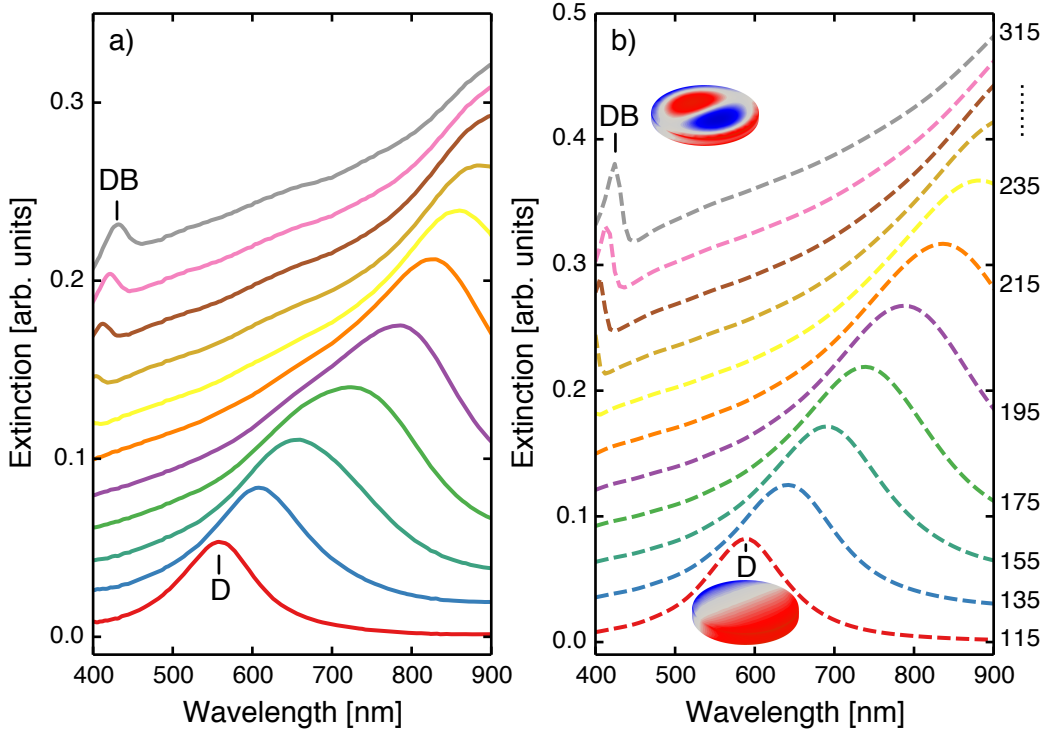


Figure 4.6.: Extinction spectra of nanodisks 115–315 nm in diameter (as indicated on the right-hand side) and 30 nm in height at normal incidence for unpolarized light. For clarity the respective spectra are vertically displaced. a) Measurement of arrays (particle spacing of $1.2\ \mu\text{m}$), b) BEM simulation ($n_{\text{eff}} = 1.30$). The surface charge distributions correspond to the dipole (D) and double breathing modes (DB).

where the form factor L_j contains the information about the aspect ratio. For spheres $L_j = 1/3$ this is the well-known *Fröhlich condition* [16] (see Eq. 2.16). For oblate particles, the form factor is decreasing with aspect ratio, $L_j < 1/3$. Consequently, the dielectric function $\varepsilon(\omega)$ that fulfills the resonance condition is shifted to more negative values. If we consider the Drude dielectric function in Fig. 2.1, we see that the resonance frequency ω is also decreasing, the result is a spectral red-shift of the resonance.

Equation 4.3 relies on the validity of the quasi-static approximation, i.e., the diameter must be considerably smaller than the wavelength ($d \ll \lambda$). This condition can be considered as satisfied by nanodisks with 100 nm diameter, but is certainly not the case for the larger diameters. For larger

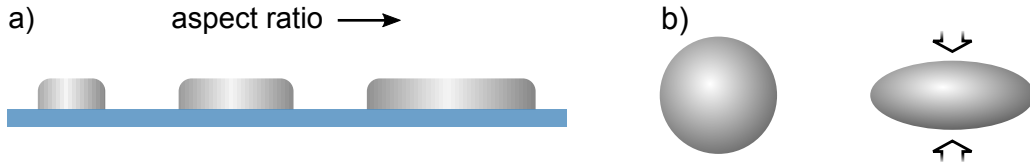


Figure 4.7.: Particle shapes. a) The aspect ratio increases with nanoparticle diameter. b) A sphere can be morphed into an oblate ellipsoid by flattening. This shape is a good approximation of the nanodisk geometry.

particles, we have to take field retardation into account. Retardation does not only give rise to an additional red-shift [43], but also to other size dependent effects as we shall see in the following sections.

Figure 4.6 b) summarizes the simulated spectra corresponding to the measurements in a). The shape of the spectra and the peak positions are perfectly reproduced. As discussed before, the simulated dipole peaks are slightly red-shifted compared to the measurement due to the choice of $n_{\text{eff}} = 1.30$. The second peak below 500 nm is identified via its surface charge map (inset) as the *double breathing* mode (DB) from the EELS measurements in Fig. 4.2, subfigure E. Due to the fact that it can be excited at normal incidence, we conclude that this mode has a non-vanishing net-dipole moment.

4.2.3. Symmetry breaking

From now on we use a tiltable sample holder to set the angle of incidence θ as shown in Fig. 3.3. First, the incident light is unpolarized. The angular dependence of the extinction spectra is summarized in Fig. 4.8 a) where spectra of the same array of nanodisks (215 nm in diameter) acquired at different angles of incidence are plotted. For a non-zero angle of incidence, a peak at a wavelength of 468 nm (labeled Q) appears in the spectrum. In contrast to the extinction of the dipole peak (D) which decreases in peak height with increasing angle, (Q) becomes stronger signifying an increasing interaction strength with the incoming light. Again, with the help of the surface charge map in Fig. 4.8 b) we are able to unambiguously identify the (dark) plasmonic quadrupole. Furthermore, the simulation hints at the existence of other dark modes (breathing mode (B) and hexapole (H)). As any peaks are too small in the measurement, we proceed and address this issue in the following chapter.

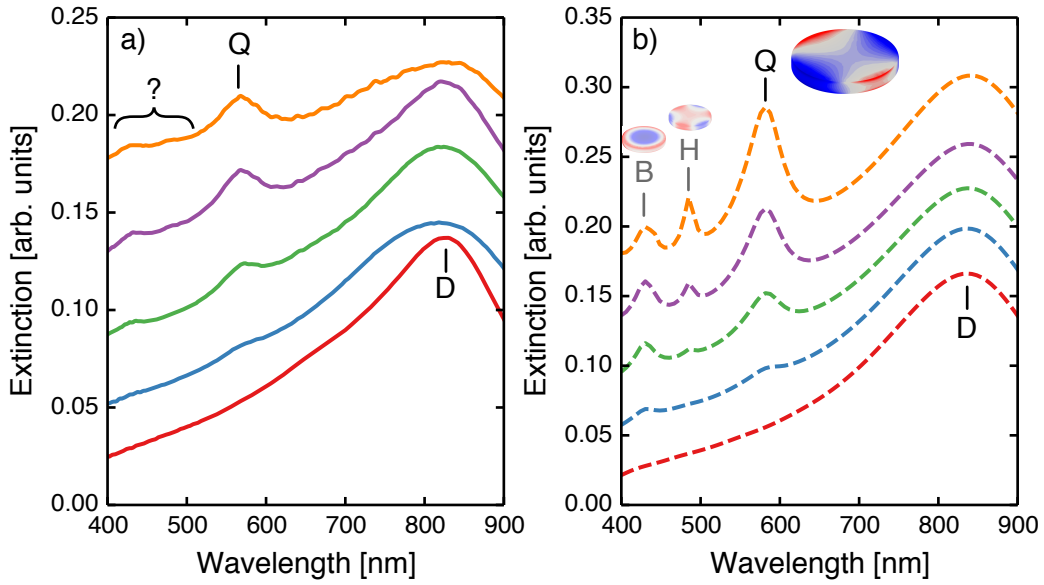


Figure 4.8.: Extinction spectra of nanodisks 215 nm in diameter and 30 nm in height at incident angles θ from 0° to 60° for unpolarized light. For clarity the respective spectra are vertically displaced. a) Measurement of arrays (particle spacing of $1.2 \mu\text{m}$), b) BEM simulation ($n_{\text{eff}} = 1.30$). The surface charge distribution corresponds to the quadrupole mode (Q). The semi-transparent surface charge maps show breathing mode (B) and hexapole mode (H).

We continue with discussing symmetry breaking due to oblique incidence and show that the excitation of the quadrupole mode can be accordingly explained. In Fig. 4.9 a) a nanoparticle at normal incidence is depicted. Although its length is in the order of the wavelength, the electric field vector is rather constant throughout the particle at a given moment. Because of the symmetry imposed by the incident plane wave, it can only couple to plasmonic modes with a (net) dipole moment.

In Fig. 4.9 b), the breaking of the quasistatic approximation together with a symmetry breaking tilt angle leads to field retardation, so that the electric field varies significantly along the particle length. By looking at the projection of the electric field vectors onto the long particle axis we understand how plasmonic modes with vanishing dipole moments can be excited. For the given example, at a certain instant, the charges are pushed simultaneously to the inside (or the edges) of the nanoparticle. For certain

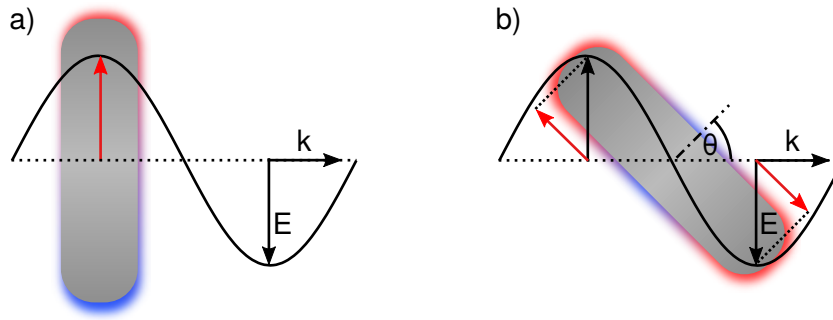


Figure 4.9.: The importance of tilt angle for the electric field retardation. a) At normal incidence, the electric field vector \mathbf{E} is rather constant across the nanodisk, even for (laterally) large nanoparticles. b) At a nonzero angle of incidence θ , this is not the case anymore, phase retardation becomes important and plasmonic modes with no net-dipole moment can be excited by incident plane waves. The red arrows are the field components along the disk diameter.

frequencies this leads to the excitation of otherwise *dark* plasmonic modes. In other words, if at least one particle dimension is large in respect to the light wavelength λ , and the wave vector \mathbf{k} has a nonzero component in this direction, electric field retardation can lead to the excitation of dark modes.

In analogy to the extinction spectra for normal incidence in Fig. 4.6, in Fig. 4.10 a similar measurement for an angle of incidence of $\theta = 30^\circ$ is plotted, again for nanodisks 115–315 nm in diameter. As before, the dipole (D) and double breathing mode (DB) are clearly visible, just with lower extinction values as expected due to the inclined illumination condition. For the quadrupole (Q) for increasing nanodisk diameter we find that the extinction increases and broadens, both can be explained by the higher radiative losses due to increased nanodisk size. The red-shift of the resonance wavelengths with increasing particle aspect ratio holds for all identified peaks.

In the simulated spectra plotted in Fig. 4.10 b), additional peaks are visible that indicate the presence of the plasmonic breathing mode (B) and the Hexapole (H), being however barely visible in the experiment. This motivates us to use polarized incident light in the following section in the hope that a more differentiated excitation results in increased relative peak intensities.

4.2.4. Polarization dependence

By combining the tiltable sample holder with a polarizer we can set the direction of the electric field vector of the incident light relative to the nanodisk axes. The nomenclature concerning the polarization (E_s, E_p) and tilt angle θ can be found in the schematic of the extinction setup in Fig. 3.3.

In Fig. 4.11 a) extinction spectra of nanodisks 200 nm in diameter and 30 nm in height are shown for angles of incidence of 0° and 45° and different polarization directions. The quadrupole mode (Q) exhibits little polarization dependence. In contrast, there is a stronger polarization-dependent peak (B) at 422 nm, that is only visible for p-polarization. Its position complies well with the p-polarized spectra in the simulation, according to the corresponding surface charge (inset) it is the plasmonic *breathing mode* (B). From the polarization dependence it becomes clear why it is less pronounced in the unpolarized illumination (see previous section). For unpolarized light its extinction is smaller relative to the background, i.e., the tail of the dipole mode. This peak is even stronger in the extinction spectrum of the nanodisks with 300 nm in diameter in Fig. 4.11 b), presumably because the field retardation is larger. The double breathing mode (DB) is only visible at normal incidence ($\theta = 0^\circ$), in accordance with the simulation.

The hexapole mode (H) in the simulation is visible for both polarization directions in inclined incidence, albeit it is stronger for s-polarized light. This weak polarization dependence and its low extinction are most likely the reason why it cannot be clearly identified in the measurement.

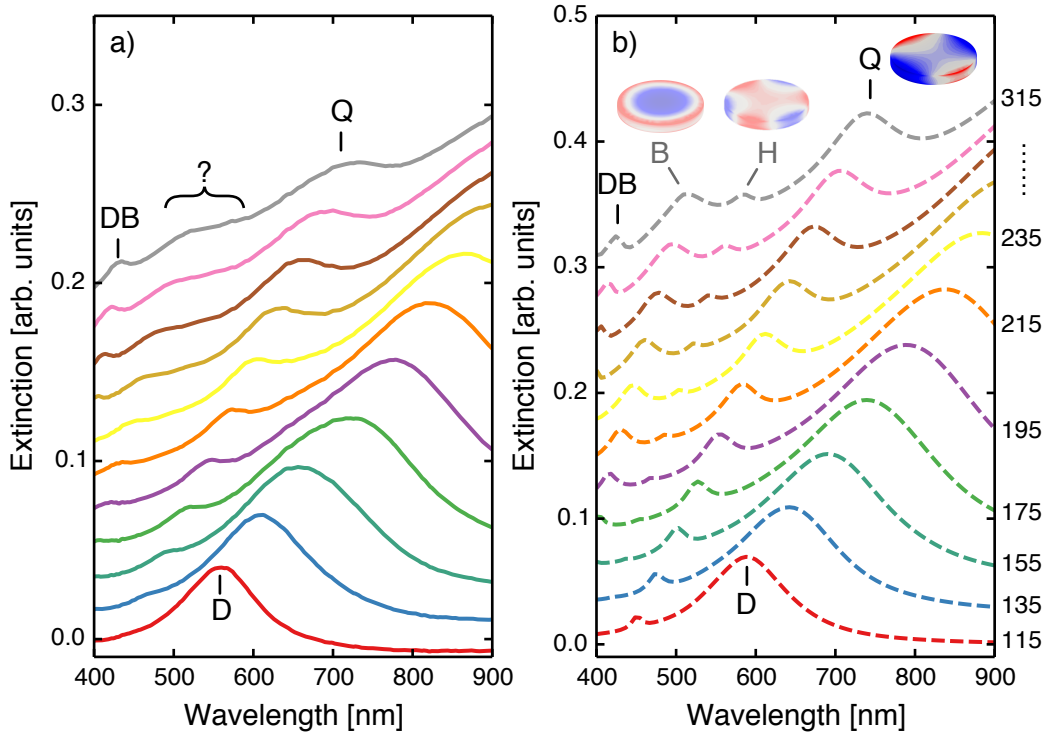


Figure 4.10.: Extinction spectra of nanodisks 115–315 nm in diameter (as indicated on the right-hand side) and 30 nm in height at oblique incidence $\theta = 30^\circ$ for unpolarized light. For clarity the respective spectra are vertically displaced. a) Measurement of arrays (particle spacing of $1.2 \mu\text{m}$), b) BEM simulation ($n_{\text{eff}} = 1.30$). The surface charge distributions correspond to the quadrupole mode (Q). The semi-transparent surface charge maps show breathing mode (B) and hexapole (H).

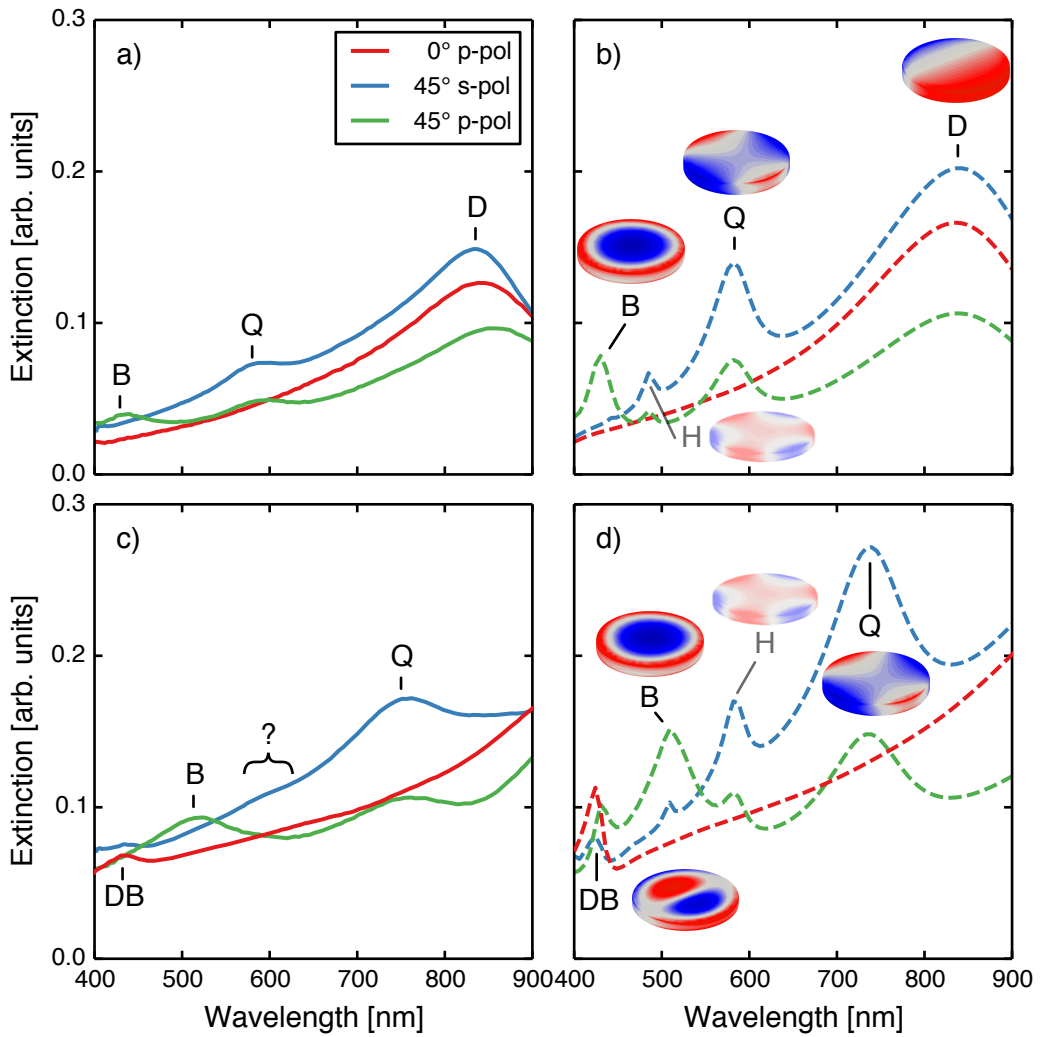


Figure 4.11.: Extinction spectra of nanodisks 30 nm in height at defined angle of incidence θ of 0° and 45° , and defined polarization: a) nanodisks 215 nm in diameter and c) for nanodisks 315 nm in diameter. The corresponding BEM simulations are plotted in b) and d) respectively, the y-axis units match the measurement. The surface charges correspond dipole (D), quadrupole (Q) and breathing mode (B). The semi-transparent surface charge maps show the hexapole mode (H).

4.3. Plasmonic edge and film modes

We now attempt to put our findings into a bigger context and introduce a concept that stems from the interpretation of EELS measurements [5]. The idea is that the multipolar plasmonic modes (dipole, quadrupole, etc.) belong to a fundamentally different mode family than the nanodisk breathing modes, and therefore, possess a distinct dispersion relation.

To emphasize the different symmetries of multipolar and breathing modes we adapt a naming convention used by Schmidt et al. [5], similar to the descriptions of mechanical vibration modes of a disk or membrane. In the said work, modes are named with respect to the number of node lines in the azimuthal and radial directions: (number of radial node lines, number of azimuthal node lines). These node lines are drawn with dotted lines in Fig. 4.12, where the dipole is denoted (1,0) and the breathing mode (0,1). It becomes clear why the double breathing mode (1,1) is referred to as a hybrid mode: it has one node line in common with both, breathing and dipole mode. Here, we are only concerned about modes that are visible in the optical measurement, but in principle higher order multipolar modes (hexapole, octupole, etc.), higher order breathing modes and combinations exist. However, they tend to be at too short wavelengths for optical characterization or their extinction cross sections are too small to be visible.

We find that the surface charges of multipolar modes are partitioned along the edge. Counting surface charge nodes along the disk circumference, we assign a plasmon wavelength λ_{SP} as the distance between the nodes, drawn with a dash-dotted line in Fig. 4.12. We thus relate the plasmon wave-

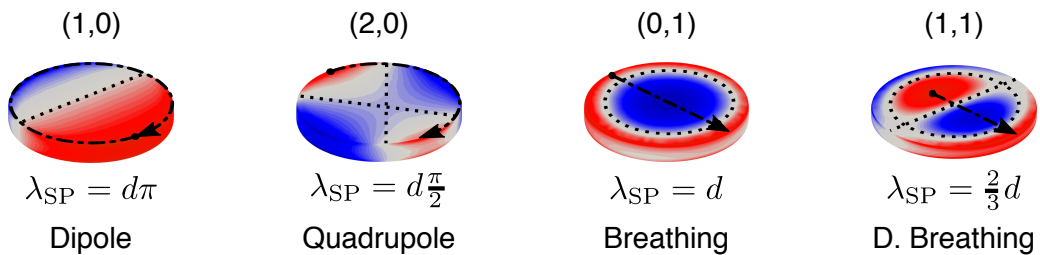


Figure 4.12.: Surface charge maps of plasmonic modes. The node lines, from which the mode notation (in parenthesis) is derived, are drawn as dotted lines. The plasmon wavelength λ_{SP} is drawn as a dash-dotted line and its relation to the disk diameter d is indicated.

length to the nanodisk diameters. Plasmonic breathing modes, on the other hand, are interpreted as standing plasmon waves confined by the edges of the disks [5]. Here, we define the plasmon wavelength λ_{SP} as the distance between charge maxima in radial direction.

The plasmon dispersion relation combines the plasmon wave number $k = 2\pi/\lambda_{\text{SP}}$ with the energy corresponding to the resonance wavelength according to $E [\text{eV}] = 1240 [\text{eV nm}]/\lambda_{\text{res}} [\text{nm}]$. Figures 4.13 a) and b) compare dispersion relations for plasmonic breathing modes obtained from EELS measurements [5] and optical spectroscopy of nanodisk arrays to the analytical film (surface) plasmon dispersion relations for the respective interfaces. It is remarkable that all data points for the optical and EELS measurements lie along a single curve and coincide perfectly with the film plasmon dispersion relation for a wide range of nanodisk diameters. This is a strong indication for the validity of the assumption that breathing modes are in fact confined surface plasmon modes.

In an attempt to extend these considerations to the multipolar modes, we include the multipolar modes and the double breathing mode (see Fig. 4.13 c)) From these modes, the dispersion relation for the double breathing mode (purple triangles) is closest to the analytical surface plasmon dispersion relation line, which highlights the close relation to the breathing mode. The quadrupole mode dispersion relation (blue triangles) differs significantly from the surface plasmon dispersion relation for higher wave numbers k , whereas it shows an asymptotical behavior for lower wave numbers. This illustrates the differences between multipolar and breathing modes. Concerning the dipole mode dispersion relation (blue squares), we note that the respective resonance wavelengths are difficult to assess, because of the broadness of the extinction peaks that are particularly susceptible to grating effects (see Fig. 4.10 a)). This has been considered in the uncertainty analysis. A direct comparison of the multipolar modes is only possible for the wave vector range of 12.7 to $17.4 \mu\text{m}^{-1}$ where dipole and quadrupole dispersion relations overlap. While their trend is similar, there is an offset between the two dispersion relations so that they barely coincide within the uncertainty. Possible explanations, such as the varying influence of the dielectric substrate on the different plasmonic modes exist, but further measurements are needed to clarify this.

To conclude, we are encouraged by the agreement of the breathing and double breathing mode with the surface plasmon dispersion relation, which suggests that both can be regarded as film plasmons. However, with the difficulties for the optical approach, EELS measurements, allowing a direct measurement of the plasmon wavelength and energy, are better suited to

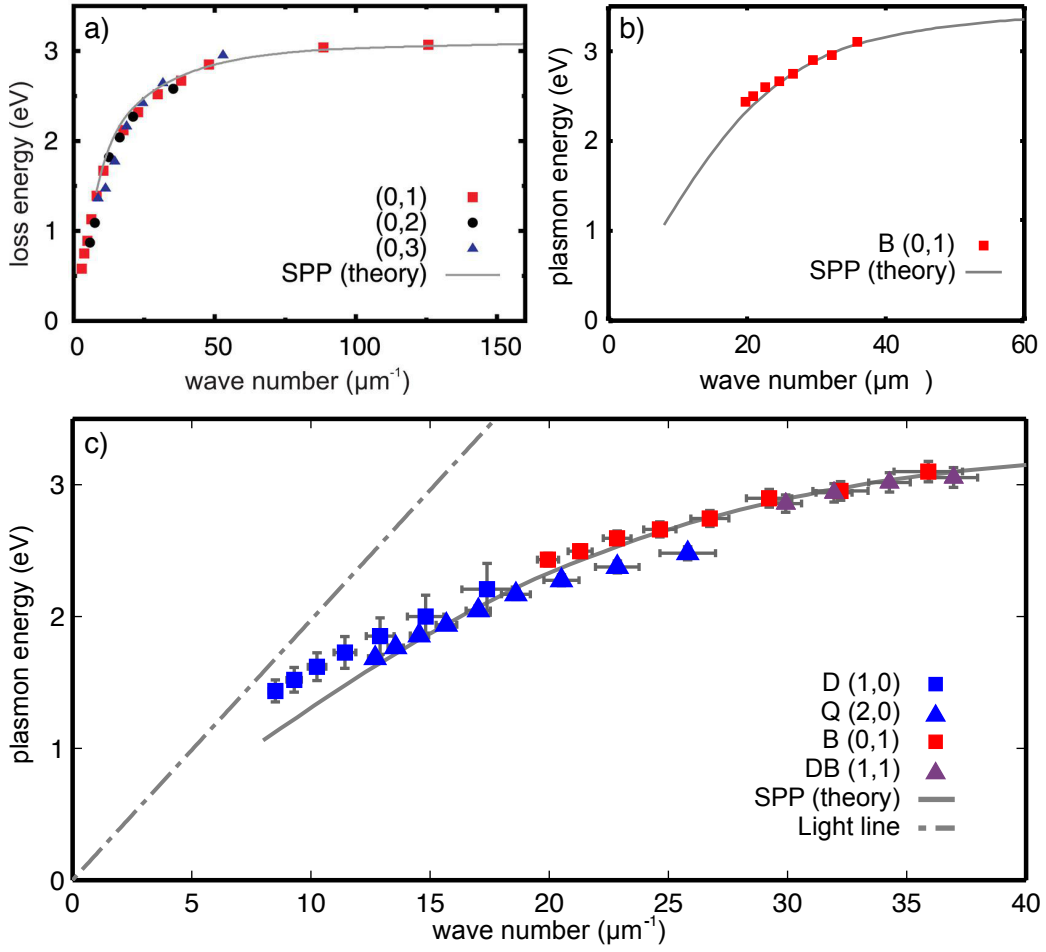


Figure 4.13.: Dispersion relations of plasmonic modes. a) EELS measurements comparing the plasmonic breathing modes to the analytical surface plasmon polariton (SPP) dispersion relation obtained by applying Fresnel equations to the silver/silicon nitride interface of a 30 nm silver and 30 nm silicon nitride multilayer [5]. b) Equivalent comparison for data from optical measurements and the analytical dispersion relation for the silver/fused quartz interface for 30 nm silver film thickness. c) Analogue to b) but showing all plasmonic modes visible in the optical measurements (see Fig. 4.10), i.e, dipole D (1,0), quadrupole Q (2,0), breathing B (0,1), and double breathing mode DB (1,1). The light line is the dispersion relation for light in vacuum. The error bars for wave vector k and Energy E are calculated by propagation of the uncertainties for the nano-disk diameters of ± 7 nm and the reading accuracy (± 50 nm for the dipole mode and ± 10 nm for the remaining modes) of the resonance wavelength λ_{res} , respectively.

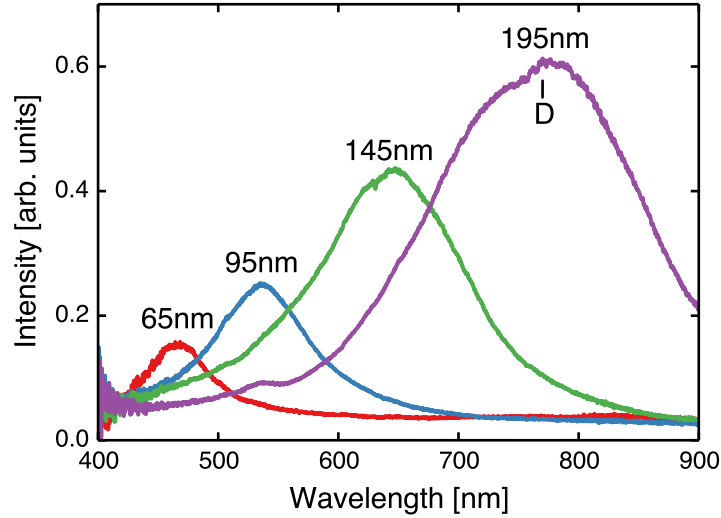


Figure 4.14.: Single particle scattering spectra of nanodisks 65–195 nm in diameter and 30 nm in height. The peaks correspond to the dipole mode (D). The numbers give the nanodisk diameters.

relate the dispersions of plasmonic modes. A current research goal is to demonstrate a common dispersion relation for multipolar plasmon modes, and to show its concurrence with the dispersion of plasmonic excitations of *straight edges*, in the same way as breathing modes relate to film plasmons. In this way, a general ordering scheme could be introduced that reduces particle plasmon modes to plasmonic excitations of extended metallic surfaces or their edges, i.e., *film* or *edge modes*.

4.4. Optical spectroscopy of single nanodisks

The single particle spectroscopy technique described in section 3.3 allows the optical characterization of individual nanostructures. It is an elegant, but experimentally demanding technique, compared to the previous measurements of nanoparticle arrays. We measure scattering spectra of single silver nanodisks 65–315 nm in diameter and 30 nm in height with an interparticle spacing of of $3\ \mu\text{m}$ on fused quartz substrate.

In Fig. 4.14 we observe a familiar red-shift of the dipole mode with increasing disk diameter due to the increasing particle aspect ratio. In addition, an increase of the scattered light intensity due to the increase in particle vol-

ume is observed. Upon comparison with the array measurements (Fig. 4.6 a) and Fig. 4.10 b)) we find that the positions of the dipole peaks match, and that the shapes are more symmetric for the single particle spectra, in fact more similar to the theoretical predictions in Fig. 4.6 b) and Fig. 4.10 b). We attribute this to the absence of grating effects due to the large inter-particle spacing. Even though in the single particle spectroscopy setup the excitation light is at an oblique incident angle, compared to the inclined measurements in Fig. 4.10, we cannot observe modes other than the dipole mode. Motivated by the results for the polarization dependent measurements in section 4.2.4 we introduce a polarizer. In addition, we limit the measurement to a small wavelength range. This avoids problems with chromatic aberration of the microscope objective because we optimize the focus for the specific wavelength range. It also enables us to match the exposure time to the low intensities of the dark modes. With these optimizations we find a peak in the scattering spectrum in Fig. 4.15 a) that is red-shifted and growing for increasing particle diameter. The spectral positions coincide with the plasmonic breathing modes in the simulation (see Fig. 4.10) and the vanishing scattering intensity for s-polarized excitation supports this interpretation (see Fig. 4.11). We thus conclude to have successfully optically probed the breathing mode of single nanodisks.

Next, we address the question of potential variations between different individual nanodisks on the basis of p-polarized spectra. Figure 4.16 depicts a direct comparison of the nanodisk spectra in Fig. 4.15 a) with spectra from nanodisks of the same nominal diameter. Here, the variation of the scattering spectra between different particles is low, which proves the effectiveness of the EBL sample fabrication.

To summarize, we have shown a means to measure the dark breathing mode of individual nanodisks. Together with the good reproducibility of the results this provides a stable basis to assess the coupling of QDs to nanodisks in the following section.

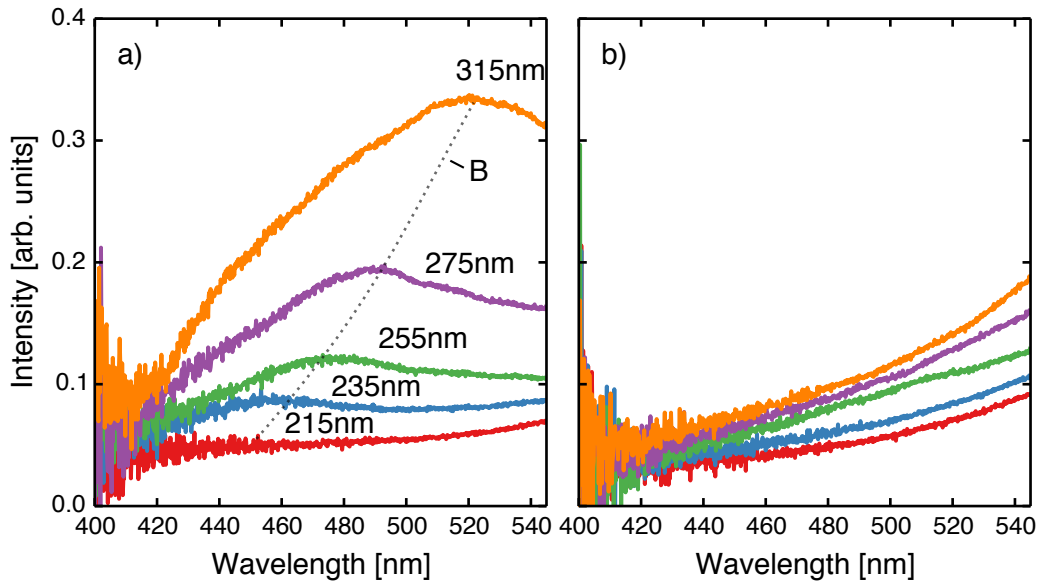


Figure 4.15.: Single particle scattering spectra of nanodisks 215–315 nm in diameter and 30 nm in height for a) p-polarized and b) s-polarized incident light. The peaks in the p-polarized measurement correspond to the plasmonic breathing mode (B) that cannot be excited with s-polarized light. Both data sets were acquired from the very same nanodisks. The dotted line connects the peaks corresponding to the breathing mode (B) as a guide to the eye.

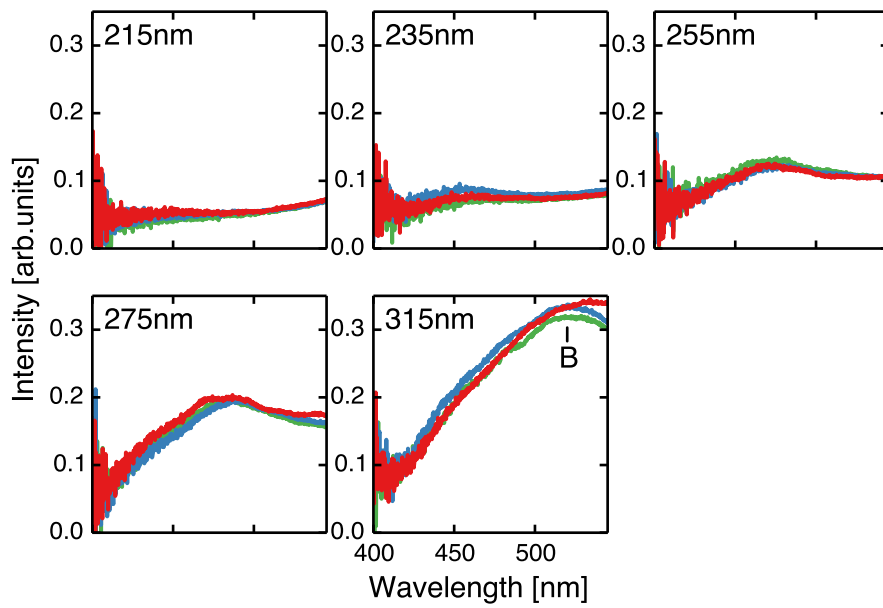


Figure 4.16.: Single particle scattering spectra of nanodisks 215–315 nm in diameter and 30 nm in height for p-polarized incident light. In each panel the spectra of three nominally identical nanodisks are plotted, so that the variation of the individual spectra can be assessed. The numbers give the nanodisk diameters.

5. Coupling of quantum dots and nanodisks

So far we have studied plasmonic nanostructures by far-field illumination. A different approach is the use of electric dipole emitters, such as fluorescent molecules or QDs, in the vicinity of the nanostructures. As explained in section 2.5 these emitters couple to plasmonic nanostructures via their electromagnetic near-fields. Because the near-field profile varies rapidly, symmetry restrictions are relaxed (in contrast to plane light waves) and we expect that dark modes can be excited too [13].

The low radiation damping of dark modes signifies high enhancement factors but as well a low coupling to the optical far-field [7]. However, because plasmonic breathing modes for here considered nanodisk diameters are not completely dark (as evident from the single particle scattering measurements in section 4.4) we can expect to see far-field signatures of a dipole emitter if it is coupled to the plasmonic nanodisk. In particular, we are motivated by the picture of the spectrally selective coupling of an emitter to a plasmonic nanostructure [14] (in our case a weakly damped breathing mode) and ask for the spectral signature observed in the far-field.

Here, we investigate the coupling of colloidal semiconductor QDs to the plasmonic breathing mode of silver nanodisks. Using the breathing mode peaks for nanodisks 315 nm in diameter in Fig. 4.11 c) at a wavelength of 515 nm as a reference, we chose QDs¹ with an emission wavelength of 533 nm. As in the designated structures the nanodisks will be covered by a total thickness of 20 nm of silicon dioxide (SiO₂) (to embed the QDs), we have to account for a red-shift of the resonance wavelength of the nanodisks of a few 10 nm. We compensate for this unknown shift by fabricating nanodisks with several diameters.

5.1. Fabrication of hybrid structures

The structures are created in a two-step electron beam lithography process, that combines the fabrication of metallic nanostructures with the determin-

¹CANdot® Series A core/shell/shell

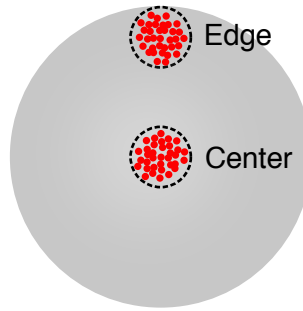


Figure 5.1.: Schematic of the positions of QD patches on silver nanodisks.

istic positioning of colloidal QDs (see section 3.1). For a systematic study, we use silver nanodisks with diameters from 115 to 415 nm and a height of 30 nm with QDs positioned within areas approximately 65 nm in diameter in the center and at the edge of the respective nanodisks, as shown schematically in Fig. 5.1.

To avoid quenching (Ohmic losses) of the QD fluorescence, the silver nanodisks and the QDs are separated by a thermally evaporated 10 nm spacer layer of SiO_2 . For protection, an additional layer of 10 nm SiO_2 is deposited on top of the QDs, so that the whole structure is embedded. SEM images of the resulting structures are shown in Fig. 5.2. The images were taken after the optical characterization and chromium had been thermally evaporated with a mass thickness of 3 nm for conductivity. We see a successful positioning, where the QDs have been deposited within circular areas of 65 ± 5 nm diameter. The number of QDs in these patches is discussed in the appendix section A.2.2. From TEM images and geometric considerations the maximum number of QDs is calculated to be 100–150 for a single layer. However, because of variations in the deposition and because of possible stacking of aggregated QDs, this number is only a rough estimate.

5.2. Spectroscopy of hybrid structures

In the following, we first characterize the QDs and silver nanodisks individually, before we focus on the combined structures. Scattering spectra of silver nanodisks are measured by single particle spectroscopy, see section 3.3, and fluorescence spectra of QDs are taken with the setup introduced in section 3.4. Figure 5.3 shows an overview of fluorescence spectra of QD patches that were deposited directly on the quartz substrate. The total fluorescence intensity in Fig. 5.3 a) varies by a factor of about 3 between the different

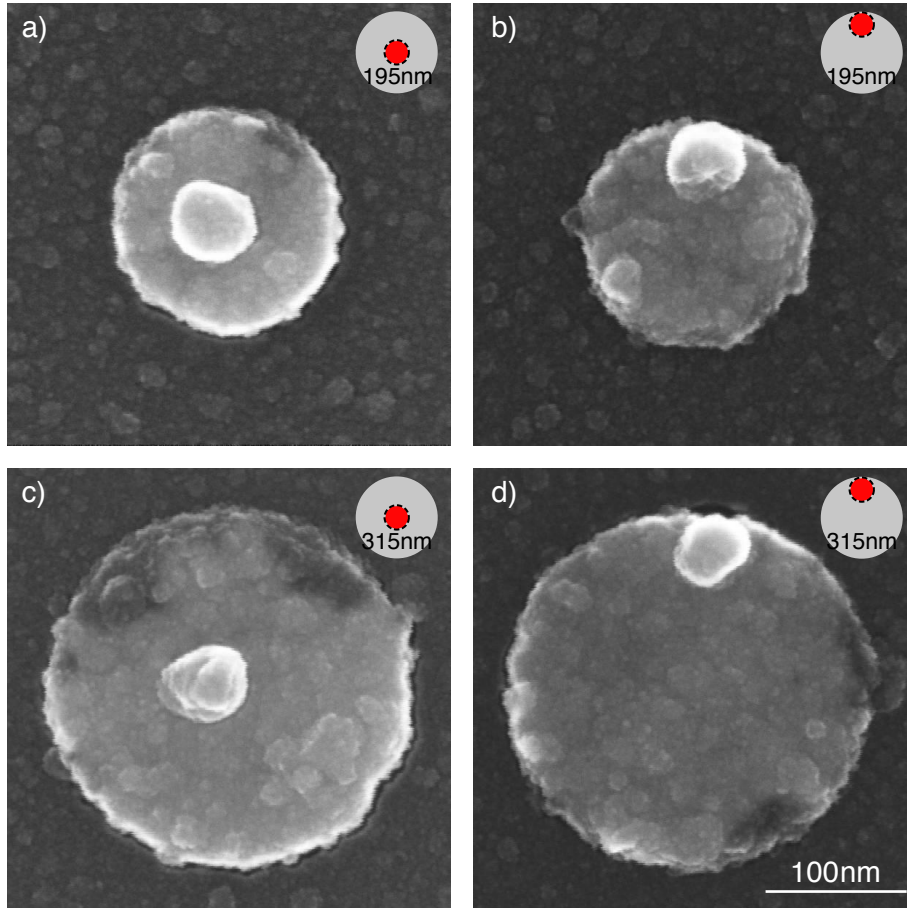


Figure 5.2.: SEM images of silver nanodisks with diameters of (a,b) 195 nm and (c,d) 315 nm. The bright spots in the center and at the edge of the nanodisks are ensembles of ≈ 100 –150 QDs. The insets indicate the nanodisk diameters and the QD positions.

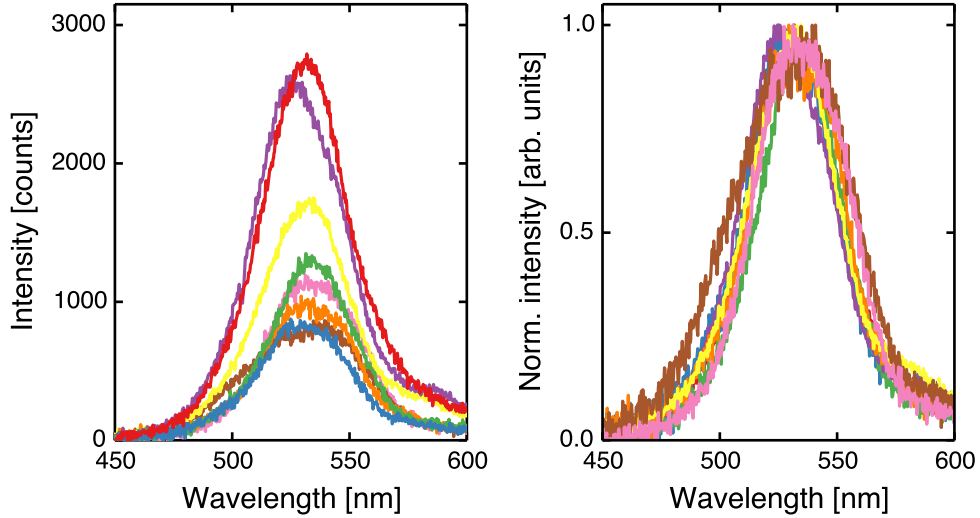


Figure 5.3.: Fluorescence spectra of different QD patches 65 ± 5 nm in diameter. The spectra plotted in a) are normalized to 1 in b).

patches which is an indication for a varying number of QDs (but includes, e.g., different orientations as well). Upon examination of the same spectral data normalized to 1 in Fig. 5.3 b), a small spectral distribution of a few nm between the QD patches can be recognized, most likely due to an inherent size distribution of the QDs.

Concerning the scattering spectra of single nanodisks embedded in SiO_2 , we however observe large variations in intensity and spectral positions between nanodisks of the same nominal diameter. These results plotted in Fig. 5.4 contrast the earlier single particle scattering measurements in Fig. 4.16. In the SEM images in Fig. 5.2, no specific fabrication issues can be recognized. The variations are most likely to the influence of the 20 nm film of SiO_2 . Irregularities on the surface of the silver nanodisk (lift-off defects), lead to high local fields – so-called hot-spots – which in turn causes a selective sensitivity to the dielectric function within close range. The differing surface features between otherwise identical nanodisks can lead to different spectral shifts by the SiO_2 , causing a spectral variation between the nanodisks.

By averaging the spectra of nominally identical nanodisks as shown in Fig. 5.4, the variations cancel out to a certain degree. Comparing the averaged spectra in Fig. 5.5 to the single particle spectra in Fig. 4.15 (or the

simulation for the 315 nm nanodisks in Fig. 4.11 b)) gives an indication for the presence of the plasmonic breathing mode. An average red-shift of approximately 25 nm is most likely due to the presence of the SiO₂.

Because of the variations in the individual nanodisk spectra, a systematic characterization of the single spectra is difficult to accomplish. In a comparison of scattering and fluorescence spectra of 160 structures (16 different nanodisk sizes with 115–415 nm diameter and QDs positioned in the center and at the edge) it consequently is not possible to find a consistent spectral modification from the plasmonic spectrum in the QD emission. Figure 5.6 shows exemplary spectra for selected geometries. First, we plot in green as a reference an averaged spectrum over many QD patches positioned on SiO₂ without nanodisks. Second, we plot in blue the QD emission of the individual QD patches (upon excitation with laser light with an emission wavelength of 375 nm) and in red the single particle scattering spectra of the respective nanodisks. Here, the idea is to compare the shape of the QD fluorescence spectra to the undisturbed average QD emission to see if the shapes of the nanodisk scattering spectra are reflected in the fluorescence emission.

In this example we do not observe a distinct peak for nanodisks 195 nm in diameter. There are however candidate peaks for the plasmonic breathing modes for the nanodisks 315 nm in diameter (compare Fig. 5.5) that coincide with the QD emission wavelength. In selected cases an asymmetric shape of the QD emission for the QDs in the nanodisks 315 nm in diameter can be identified, although, from a full comparison with other diameters this is not corroborated.

Their main difficulties here are the spectral variations that are already apparent for the (nominally identical) uncoupled structures. This includes the scattering spectra (Fig. 5.4) affecting the systematic comparison, and the, albeit smaller, variations of the QDs emission (Fig. 5.3) which complicates the finding of a spectral signature. In Fig. 5.6, the scattering intensity for the nanodisks 215 nm in diameter is not significantly lower than for the nanodisks 315 nm in diameter. The high background stems from the tail of the quadrupole peak (which can be seen from the s-polarized single particle scattering spectra in Fig. 4.15 b)). Also problematic is the small spectral width of the used QDs compared to the plasmonic breathing mode. In previous successful approaches of QDs coupled to nanowire plasmon modes in the work by Gruber et al. [44] and the study of fluorescent molecules in the gap of gold dimers by Ringler et al. [14], the fluorescence was spectrally broader than the plasmonic modes.

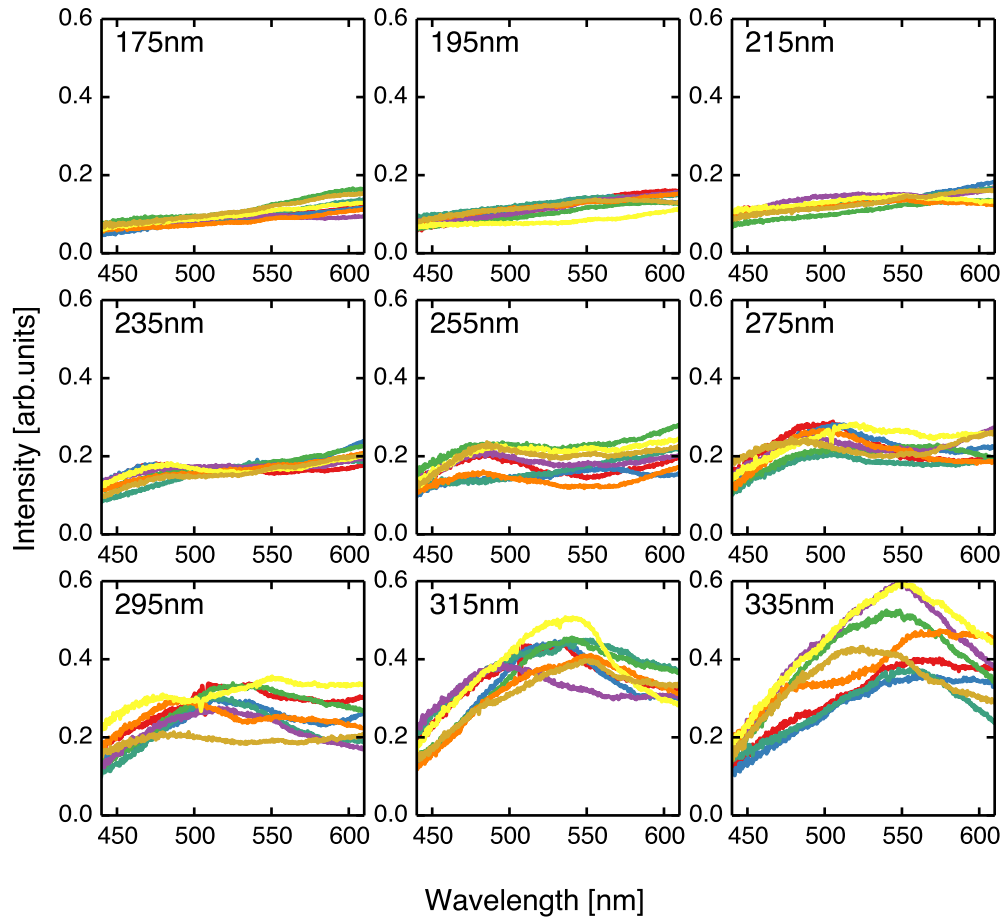


Figure 5.4.: Single particle scattering spectra of SiO_2 coated nanodisks 175–335 nm in diameter and 30 nm in height for p-polarized incident light. In each panel the spectra of 8 nominally identical nanodisks (drawn in different colors) are plotted, so that the variation of the individual spectra can be assessed. The peaks evident for the larger nanodisks can be attributed to the plasmonic breathing mode. The numbers give the nanodisk diameters.

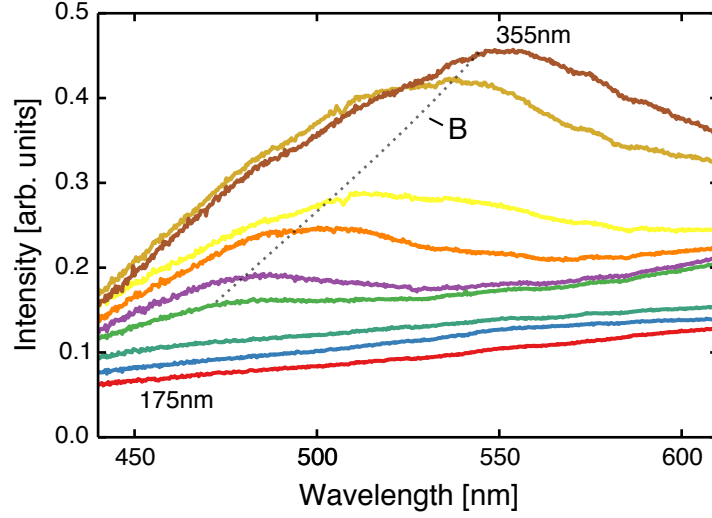


Figure 5.5.: Averaged scattering spectra of SiO_2 coated nanodisks 30 nm in height for p-polarized incident light. Nanodisk diameters range from 175 nm to 335 nm, as indicated. The spectra of the individual nanodisks are plotted in Fig. 5.4 and averaging has been done by summation and normalization by the number of averaged spectra. The dotted line connects the peaks corresponding to the breathing mode (B) as a guide to the eye.

To summarize this section, we have demonstrated the successful fabrication of the required hybrid structures and shown a way to measure both, the QD fluorescence and the scattering of the plasmonic nanodisk of individual structures. So far, the ambitious goal of measuring a spectral signature of the coupling of emitters to the dark plasmonic mode could not be met. However, improvements in the sample design might provide the right platform to do so.

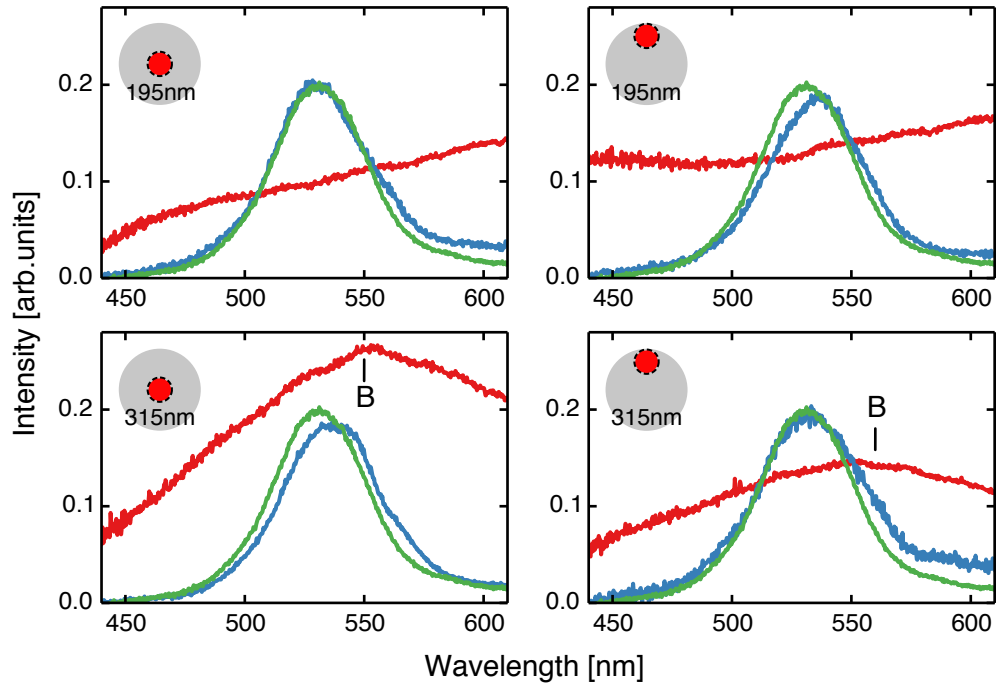


Figure 5.6.: Selection of fluorescence (blue) and scattering (red) spectra of single structures from QDs and silver nanodisks. The fluorescence spectra are compared to a spectrum (green) averaged over many QD patches without nanodisks, to assess if plasmon-related changes in the QD emission are visible. Both fluorescence spectra are normalized to facilitate the comparison. The nanodisk diameters and the positions of the QDs are indicated by the insets, candidates for the breathing mode are labeled (B).

5.3. Fluorescence lifetime measurements

A different way to assess the coupling of emitters and plasmonic nanostructures is by measuring the fluorescence lifetime. The shortening of the fluorescence lifetime in the vicinity of plasmonic structures is a clear indication of coupling as discussed in section 2.5. The lifetime measurements are performed with a TCSPC setup (described in section 3.5). With this technique, the emitters are excited by a short laser pulse, and the photon arrival times are recorded. From the exponentially decaying fluorescence intensity, the mean fluorescence lifetime τ can be extracted. The mean lifetime is the inverse of the decay rate, $\tau = 1/\Gamma$. The single photon counting data are shown as the number of photon counts over time, normalized to 1. Quite often non-exponential decay traces are observed. As we cannot deduce all details in QD/disk coupling we chose a simple fitting approach considering multiple time constants τ_i :

$$I(t) = \sum_{i=1}^N c_i e^{-\frac{t}{\tau_i}}, \quad (5.1)$$

where N is the total number of time constants and c_i is the statistical weight of each contribution. However, we note in passing that this approach is not relying on a physical model. Such a model is difficult to establish for the case of multiple interacting emitters, because even for single QDs multiple decay rates for different electronic transitions can exist and QD interaction in ensembles is known to cause non-exponential behavior. In our case, the description is further complicated because the symmetry breaking substrate distinguishes otherwise identical emitters by their emission dipole's (random) orientation. This gives rise to a broadening of the time constants. Figure 5.7 shows two exemplary time traces with different fit functions. It can be seen that the time trace of QDs on a dielectric substrate (SiO_2) in Fig. 5.7 a) can be well approximated by a two-exponential function, however, for the same QDs patch on a silver nanodisk in Fig. 5.7 b) this approach is not sufficient and only a three-exponential fit matches the time trace. The effect of the metal structures can be understood by the high local density of states. Furthermore, because of the local metal roughness and varying distances between QDs and metal, the environment of each QD is slightly different. From a study by Wu et al. [45] we expect the influence to increase – and lifetimes to broaden – with decreasing distance to the metal.

In absence of a simple experimentally accessible model and motivated by the adequate multi-exponential fits in Fig. 5.7 b), we use three discrete

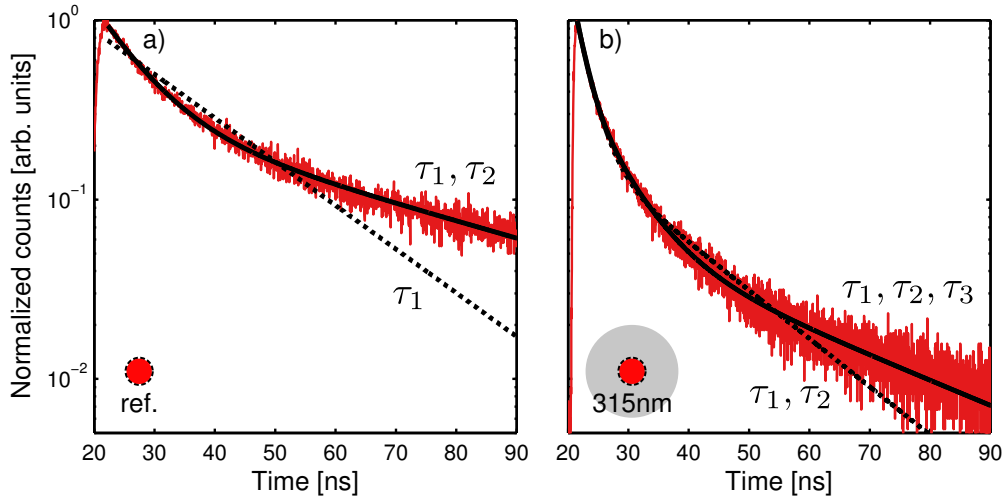


Figure 5.7.: Fluorescence time traces and exponential fits. a) Fluorescence time trace from a QD patch on SiO_2 fitted with a mono-exponential (dashed line, τ_1) and a two-exponential (solid line, τ_1, τ_2) fit function. b) QD patch on silver nanodisks (315 nm in diameter) showing a complex behavior that a two-exponential fit (dashed line, τ_1, τ_2) cannot describe, instead a three-exponential fit (solid line line, τ_1, τ_2, τ_3) is used.

time constants to classify the fluorescence time traces. It is not possible to separate these time constants because all three time constants are affected by the influence of plasmonic structures. However, the longest time constant τ_3 has a low statistical weight of only approximately 10% in all measurements. We therefore focus on the evolution of the shortest and the second shortest time constants τ_1 and τ_2 .

To study the influence of the presence of plasmonic structures, first, the undisturbed QDs are measured. The resulting time traces are shown in Fig. 5.8 a). In this and all other panels the different curves are acquired from nominally identical individual hybrid systems. An exponential fit of the fastest decaying QD patch is drawn. Panels c) to f) show the time traces of QDs on silver nanodisks. The data is grouped by nanodisk diameter and position on the nanodisks (similar to the SEM images in Fig. 5.2 and the spectroscopic data in Fig. 5.6). Here, exponential fits for the slowest decaying patches times are plotted. This enables us to conduct a worst case comparison in Fig. 5.8 b), where the fitted time traces of the QDs on nanodisks and the undisturbed QDs are directly compared with each other.

It is evident that the lifetimes are much smaller for the QD patches on the nanodisks.

To quantify the decrease in lifetime, the time constants τ_1 and τ_2 of the QD on the nanodisks and the reference QDs are averaged and plotted as a histogram in Fig. 5.9. For the case that the time constants of the undisturbed case and the coupled case match (e.g., $\tau_1 \Rightarrow \tau_1$), both are reduced by approximately a factor of three. There is the possibility that the time constant τ_1 of the undisturbed QDs corresponds to an intrinsic decay channel of the QDs which is unchanged by the coupling. This would imply that it corresponds to time constant τ_2 from the coupled case (e.g., $\tau_1 \Rightarrow \tau_2$). This in turn would signify that the time constant τ_2 matches the time constant τ_1 of the coupled case and is then shortened by one order of magnitude. We note that the values of τ_1 in the coupled case are close to the value of the width of the instrument response function of the avalanche photodetector of ≈ 1 ns, which thus sets a resolution limit. This suggests the possibility that the time constant τ_1 could be even smaller, which could mean that the differences between the nanodisk diameters and positions is actually hidden by the instrument response function. Otherwise, the findings from the previous section concerning the variations of the resonance wavelength for the plasmonic breathing mode and the large background in the scattering spectra that stem from the quadrupole mode are still valid and might explain why no significant differences for the different hybrid systems are observed.

We see that while the great advantage of the lifetime measurement is that the total time evolution can be directly measured, it is difficult to separate different decay channels without a real physical model. In any case, we have successfully proven the coupling of QDs to silver nanodisks, a promising combination that demands further research.

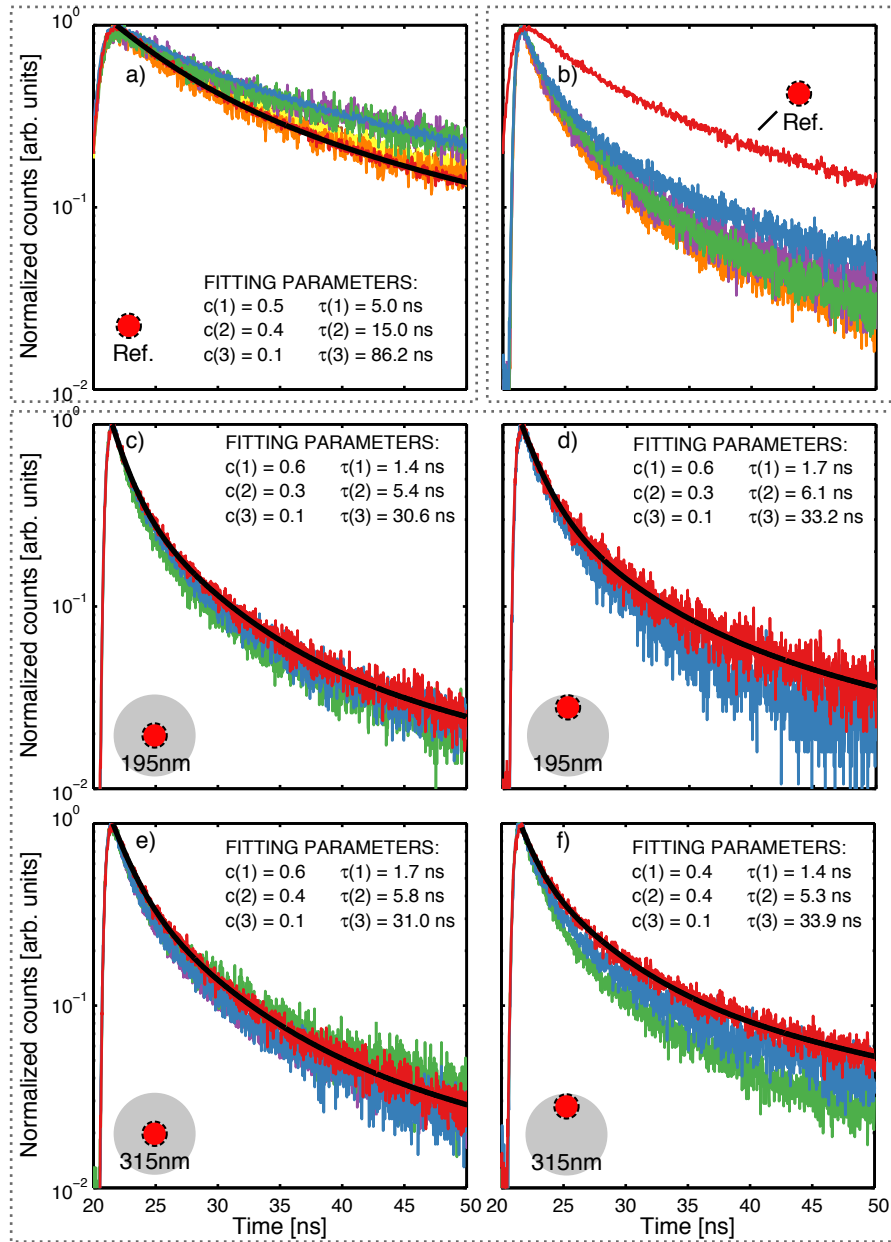


Figure 5.8.: Fluorescence time traces of QD patches, The insets indicate the nanodisk diameters and the QD positions. The fit parameter $\tau(i)$ correspond to the time constants and $c(i)$ are their statistical weights from the fit. a) Reference measurement of QD patches on SiO_2 . b) Direct comparison of the (fastest decaying and fitted) reference measurement (red line) and the QD patches on silver nanodisks from panels c) to f). In these panels, the slowest decaying QDs are fitted.

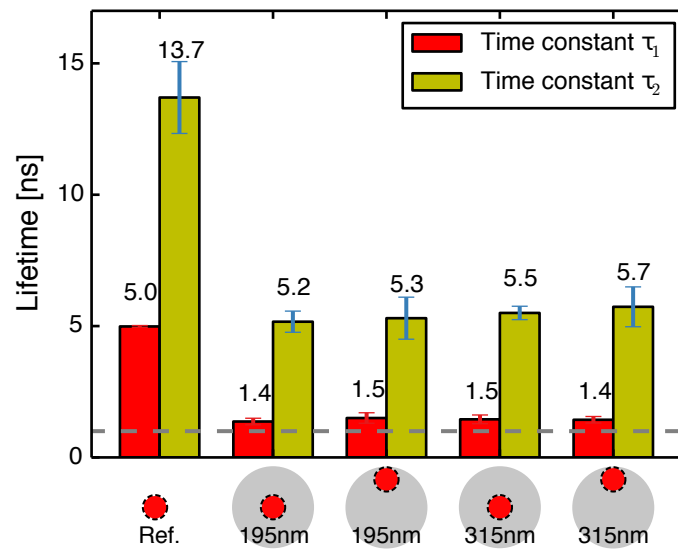


Figure 5.9.: Histogram of the fastest (τ_1) and second fastest (τ_2) time constants for different hybrid system configurations, indicated by the insets. The bars labeled “Ref.” correspond to the undisturbed QD patches.

6. Conclusion

In this thesis we demonstrate the optical characterization of dark plasmonic modes of lithographically fabricated silver nanodisks. We find that the majority of modes visible in the EELS measurements can be optically characterized by adjusting the incident angle and the polarization direction of the illumination light. The results of the spectroscopic measurements of nanoparticle arrays are in excellent agreement with numerical simulations and comparable to previous EELS measurements. Single particle scattering spectroscopy corroborates the results and it reveals minimal spectral variations of the EBL fabricated nanodisks.

If the particle dimension along the wave vector direction of the incident light is not negligibly small compared to the resonance wavelength, field retardation becomes important, because the electric field varies across the nanoparticle. Increasing the incident angle, i.e., moving away from normal incidence, breaks the symmetry of the optical excitation and enables to control the strength of the retardation. This leads to increased interaction of dark modes with the incident light.

A thorough investigation of the plasmonic mode spectrum using this principle has led to several insights. It is indeed possible to excite the plasmonic breathing mode with p-polarized incident light. In contrast, the quadrupole mode, showing lower symmetry, can be excited with s- and p-polarized light likewise. The double breathing mode, which appears to be a hybrid mode between dipole and breathing mode, can only be excited efficiently at normal incidence, which signifies that it is in fact a bright mode. The reason why it has not been observed with optical methods before is probably due to the fact that its resonance is only in the visible spectral range for large nanodisk diameters. Optical measurements reveal the subtle differences in polarization dependence and whether plasmonic modes are bright or dark. For increasing particle sizes the line between bright and dark modes blurs, because for the right conditions none of the shown modes are truly dark. Even the highly symmetric plasmonic breathing mode decays radiatively for sufficiently large nanodisks.

In the second part of this work, we demonstrate the fabrication of hybrid nanostructures using a two-step lithography process with high positioning

accuracy. These structures built from nanodisks and QD ensembles on defined positions enable us to study the interactions of emitters and plasmonic structures. A spectral signature of the plasmonic breathing mode in the QD emission due to coupling can not be shown for the given sample, because of large variations in the individual scattering spectra. These variations can be related to the influence of the 20 nm SiO₂ layer on the nanodisks in which the QDs are embedded. Because of the strong near-field in the vicinity of sharp points (*lift-off* defects) in plasmonic nanostructures, these surface features show a high local sensitivity to the refractive index of the nearby medium that contribute to the overall resonance wavelength shift. As these defects vary from particle to particle, the scattering spectra vary for nominally identical particles which inhibits a systematic study.

Complimentary fluorescence lifetime measurements are conducted. Here, the occurrence of non-exponential lifetime traces is met with fitting routines assuming multi-exponential functions. While this does not allow to distinguish between different decay processes, it nevertheless provides means to assess a change of the overall decay characteristics. We observe a shortening by at least a factor of three on the metal compared to the QDs on SiO₂ substrate, which is proof of a coupling of QDs and nanodisks.

Perspective

The successful characterization of the plasmonic mode spectrum relies mainly on the nanoparticle array measurements. Further single particle scattering spectroscopy poses an opportunity to learn more about the radiative decay of plasmonic modes on the scale of individual nanoparticles

The understanding of the coupling of QDs and nanodisks would profit from further research. Here, an understanding of the influence of the necessary SiO₂ layer is important. The observed variations in the spectral signatures of individual nanodisks can possibly be avoided by completely embedding the hybrid structure in SiO₂, forming a homogeneous environment.

The spectral shaping of the fluorescence emission for QDs coupled to dark modes remains an interesting question, especially with respect to their mutual position dependencies of the coupling to different plasmonic modes. In principle, emitter fluorescence that is spectrally broader than the plasmonic modes could be beneficial. Further characterization techniques, such as back focal plane imaging that images radiation patterns, would widen the experimental reach. Finally, further numerical simulations would provide extended reference points to gain a better understanding of the interaction of emitters and dark plasmonic modes.

Acknowledgment

It was during my year abroad in Grenoble that my interest in the optical properties of nanostructures was awakened. There, my attention was brought to the nano-optics group at the Karl-Franzens-University Graz, where I have prepared this thesis.

First of all, I am deeply thankful for the support that I have received from my supervisor, Joachim Krenn. I consider myself fortunate to have been able to profit from his experience and guidance. He has always taken his time to give me a critical opinion, an encouraging smile and a share of his vision.

Furthermore, I am grateful for the warm welcome at the nano-optics group. Without the combined knowledge from its individual members, this work would not have been possible. In particular, I want to thank Andreas Hohenau and Christian Gruber for passing on their knowledge to me. This work has also profited greatly from the helpful discussions with Ulrich Hohenester, Andreas Trügler and Michael Reisecker from the theoretical physics department at the Karl-Franzens-University Graz. I would like to thank my fellow labmates for the pleasant working atmosphere and the fun we shared. It has been an inspiring time with all of you, so far, down the rabbit hole in the wonderland of nano-optics.

Special thanks go to the kind people that have helped me to overcome the bureaucratic obstacles of writing this thesis at the Karl-Franzens University. I especially want to thank Daniela Gaar, for making every possible effort in this regard. I am also indebted to Claudia Berger and Gernot Schaffernak for proof-reading this work and providing me with valuable comments.

I am most grateful for the support and encouragement that I have received from my family, with whose help I have been able to find my own way. Finally, I thank you, Verena, not only for your moral support during my writing time but for sharing my hopes and dreams and being the wonderful person you are.

Bibliography

- [1] L. Novotny and B. Hecht, *Principles of nano-optics*. Cambridge: Cambridge University Press, 2006.
- [2] S. Lal, S. Link, and N. J. Halas, “Nano-optics from sensing to waveguiding,” *Nature Photonics*, vol. 1, pp. 641–648, Nov. 2007.
- [3] H. A. Atwater, “The promise of plamonics,” *Scientific American*, vol. 296, pp. 56–63, Apr. 2007.
- [4] W. L. Barnes, A. Dereux, and T. W. Ebbesen, “Surface plasmon sub-wavelength optics,” *Nature*, vol. 424, p. 824–830, Aug. 2003.
- [5] F.-P. Schmidt, H. Ditlbacher, U. Hohenester, A. Hohenau, F. Hofer, and J. R. Krenn, “Dark plasmonic breathing modes in silver nanodisks,” *Nano Letters*, vol. 12, pp. 5780–5783, Nov. 2012.
- [6] D. Solis, B. Willingham, S. L. Nauert, L. S. Slaughter, J. Olson, P. Swanglap, A. Paul, W.-S. Chang, and S. Link, “Electromagnetic energy transport in nanoparticle chains via dark plasmon modes,” *Nano Letters*, vol. 12, pp. 1349–1353, Mar. 2012.
- [7] M. Pelton, *Introduction to metal-nanoparticle plasmonics*. Hoboken, New Jersey: John Wiley & Sons Inc, 2013.
- [8] Z. Fang, J. Cai, Z. Yan, P. Nordlander, N. J. Halas, and X. Zhu, “Removing a wedge from a metallic nanodisk reveals a Fano resonance,” *Nano Letters*, vol. 11, pp. 4475–4479, Oct. 2011.
- [9] Y. Zhang, T. Q. Jia, H. M. Zhang, and Z. Z. Xu, “Fano resonances in disk–ring plasmonic nanostructure: strong interaction between bright dipolar and dark multipolar mode,” *Optics Letters*, vol. 37, pp. 4919–4921, Dec. 2012.
- [10] G. Schider, J. R. Krenn, A. Hohenau, H. Ditlbacher, A. Leitner, F. R. Aussenegg, W. L. Schaich, I. Puscasu, B. Monacelli, and G. Boreman, “Plasmon dispersion relation of Au and Ag nanowires,” *Physical Review B*, vol. 68, p. 155427, Oct. 2003.

- [11] F. Hao, E. M. Larsson, T. A. Ali, D. S. Sutherland, and P. Nordlander, “Shedding light on dark plasmons in gold nanorings,” *Chemical Physics Letters*, vol. 458, pp. 262–266, June 2008.
- [12] U. Hohenester and A. Trügler, “MNPBEM – a matlab toolbox for the simulation of plasmonic nanoparticles,” *Computer Physics Communications*, vol. 183, pp. 370–381, Feb. 2012.
- [13] M. Liu, T.-W. Lee, S. K. Gray, P. Guyot-Sionnest, and M. Pelton, “Excitation of dark plasmons in metal nanoparticles by a localized emitter,” *Physical Review Letters*, vol. 102, p. 107401, Mar. 2009.
- [14] M. Ringler, A. Schwemer, M. Wunderlich, A. Nichtl, K. Kürzinger, T. A. Klar, and J. Feldmann, “Shaping emission spectra of fluorescent molecules with single plasmonic nanoresonators,” *Physical Review Letters*, vol. 100, p. 203002, May 2008.
- [15] N. W. Ashcroft and N. D. Mermin, *Solid state physics*. New York: Holt, Rinehart and Winston, 1976.
- [16] S. A. Maier, *Plasmonics: fundamentals and applications*. New York: Springer, 2007.
- [17] J. D. Jackson, *Classical electrodynamics*. New York: Wiley, 1999.
- [18] C. F. Bohren and D. R. Huffman, *Absorption and scattering of light by small particles*. New York: Wiley, 1983.
- [19] G. Mie, “Beiträge zur Optik trüber Medien, speziell kolloidaler Metallösungen,” *Annalen der Physik*, vol. 330, no. 3, p. 377–445, 1908.
- [20] U. Kreibig, *Optical properties of metal clusters*. No. 25 in Springer series in materials science, Berlin: Springer, 1995.
- [21] K. L. Kelly, E. Coronado, L. L. Zhao, and G. C. Schatz, “The optical properties of metal nanoparticles: the influence of size, shape, and dielectric environment,” *The Journal of Physical Chemistry B*, vol. 107, pp. 668–677, Jan. 2003.
- [22] E. Fermi, “Quantum theory of radiation,” *Reviews of Modern Physics*, vol. 4, pp. 87–132, Jan. 1932.
- [23] W. L. Barnes, “Fluorescence near interfaces: The role of photonic mode density,” *Journal of Modern Optics*, vol. 45, pp. 661–699, July 1998.

- [24] A. Broers, A. Hoole, and J. Ryan, “Electron beam lithography—Resolution limits,” *Microelectronic Engineering*, vol. 32, pp. 131–142, Sept. 1996.
- [25] Robert W. Johnstone, *Self-sacrificial surface-micromachining using poly(methyl methacrylate)*. PhD thesis, Simon Fraser University, 2008.
- [26] A. C. Ouano, “A study on the dissolution rate of irradiated poly(methyl methacrylate),” *Polymer Engineering & Science*, vol. 18, p. 306–313, Mar. 1978.
- [27] Christian Gruber, *Controlled coupling of quantum dots to plasmonic nanowires*. PhD thesis, Karl-Franzens-Universität Graz, 2013.
- [28] B. Lamprecht, G. Schider, R. T. Lechner, H. Ditlbacher, J. R. Krenn, A. Leitner, and F. R. Aussenegg, “Metal nanoparticle gratings: Influence of dipolar particle interaction on the plasmon resonance,” *Physical Review Letters*, vol. 84, pp. 4721–4724, May 2000.
- [29] B. Augu e and W. Barnes, “Collective resonances in gold nanoparticle arrays,” *Physical Review Letters*, vol. 101, Sept. 2008.
- [30] W. Rechberger, A. Hohenau, A. Leitner, J. R. Krenn, B. Lamprecht, and F. R. Aussenegg, “Optical properties of two interacting gold nanoparticles,” *Optics Communications*, vol. 220, pp. 137–141, May 2003.
- [31] W. Becker, *Advanced time-correlated single photon counting techniques*. No. 81 in Springer series in chemical physics, Berlin: Springer, 2005.
- [32] F. J. Garc a de Abajo and A. Howie, “Retarded field calculation of electron energy loss in inhomogeneous dielectrics,” *Physical Review B*, vol. 65, p. 115418, Mar. 2002.
- [33] U. Hohenester and J. R. Krenn, “Surface plasmon resonances of single and coupled metallic nanoparticles: A boundary integral method approach,” *Physical Review B*, vol. 72, p. 195429, Nov. 2005.
- [34] K. S. Yee, “Numerical solution of initial boundary value problems involving Maxwell’s equations in isotropic media,” *IEEE Trans. Antennas and Propagation*, p. 302–307, May 1966.

- [35] H. DeVoe, “Optical properties of molecular aggregates. I. Classical model of electronic absorption and refraction,” *The Journal of Chemical Physics*, vol. 41, pp. 393–400, July 2004.
- [36] Andreas Trügler, *Optical properties of metallic nanoparticles*. PhD thesis, Karl-Franzens-Universität Graz, Graz, 2011.
- [37] F. J. García de Abajo and M. Kociak, “Probing the photonic local density of states with electron energy loss spectroscopy,” *Physical Review Letters*, vol. 100, p. 106804, Mar. 2008.
- [38] U. Hohenester, H. Ditlbacher, and J. R. Krenn, “Electron-energy-loss spectra of plasmonic nanoparticles,” *Physical Review Letters*, vol. 103, p. 106801, Aug. 2009.
- [39] M.-W. Chu, V. Myroshnychenko, C. H. Chen, J.-P. Deng, C.-Y. Mou, and F. J. García de Abajo, “Probing bright and dark surface-plasmon modes in individual and coupled noble metal nanoparticles using an electron beam,” *Nano Letters*, vol. 9, pp. 399–404, Jan. 2009.
- [40] T. Götz, W. Hoheisel, M. Vollmer, and F. Träger, “Characterization of large supported metal clusters by optical spectroscopy,” *Zeitschrift für Physik D Atoms, Molecules and Clusters*, vol. 33, pp. 133–141, June 1995.
- [41] Walter Gotschy, *Absorptionseigenschaften regelmäßig strukturierter Metallpartikelfilme*. PhD thesis, Karl-Franzens-Universität Graz, 1996.
- [42] P. B. Johnson and R. W. Christy, “Optical constants of the noble metals,” *Physical Review B*, vol. 6, pp. 4370–4379, Dec. 1972.
- [43] M. Meier and A. Wokaun, “Enhanced fields on large metal particles: dynamic depolarization,” *Optics Letters*, vol. 8, pp. 581–583, Nov. 1983.
- [44] C. Gruber, P. Kusar, A. Hohenau, and J. R. Krenn, “Controlled addressing of quantum dots by nanowire plasmons,” *Applied Physics Letters*, vol. 100, p. 231102, June 2012.
- [45] X. Wu, Y. Sun, and M. Pelton, “Recombination rates for single colloidal quantum dots near a smooth metal film,” *Physical Chemistry Chemical Physics*, vol. 11, pp. 5867–5870, July 2009.
- [46] CAN GmbH, Hamburg, “Datasheet CANdot Series A core/shell/shell SAB-0-005-02.”

A. Appendix

A.1. Fabrication parameters

1. Electron beam lithography resist

- Substrate: quartz glass, $1 \times 1 \text{ cm}^2$, cleaned according to section A.1.1
- Plasma cleaning: 15 min at the highest setting of the plasma cleaner¹.
- Resist: PMMA (polymethyl methacrylate), molecular weight 950K, 2% solid content²
- Spin coating: $30 \mu\text{l}$ at 4000 rpm for 30 s
- Resulting film thickness: $\approx 60 \text{ nm}$
- Prebake: 5 min at 180° on hotplate in air

2. Aluminum deposition

- Film thickness: 8 nm
- Deposition rate: $1 - 2 \text{ \AA/s}$
- Base pressure: $5 \times 10^{-6} \text{ mbar}$

3. Electron beam lithography parameters

- Electron acceleration voltage: 20 kV
- Aperture: $10 \mu\text{m}$
- Electron beam current: $\approx 25 \text{ nA}$
- Exposure dose for area: $350 \mu\text{C/cm}^2$
- Exposure dose for dot: 20 fC
- Write field size: $100 \times 100 \mu\text{m}^2$
- Beam speed: $\approx 1 - 2 \text{ mm/s}$

¹Harrick Plasma, PDC-3XG

²Allresist AR-P 671.02

4. Aluminum removal
 - Dip sample in sodium hydroxide solution (1 NaOH tablet per 80 ml water) until the aluminum has dissolved
 - Rinsing with deionized water
5. PMMA development:
 - Development³ : 30 s
 - Stopping⁴: 30 s
 - Rinsing with isopropanol
6. Silver film for nanodisks
 - Film thickness: 30 nm
 - Deposition rate: 10 Å / s
 - Base pressure: 5·10⁻⁶ mbar
7. Positioning of QDs
 - CANdot® Series A core/shell/shell in toluene
 - Concentration: 50 μmol / l
 - Spin coating: 10 μl at 4000 rpm for 30 s
 - Plasma cleaning: 30 s at medium setting
8. Lift-off
 - 3 h in acetone at 45°
 - Rinsing with isopropanol

A.1.1. Cleaning procedure

This is a recipe for a mechanical cleaning procedure that works well if the substrate is already reasonably clean. It has the advantage of not needing to immerse the substrates in a cleaning solution. The draw-back is that only the center of the sample is cleaned.

1. Start the procedure with the downside of a substrate and repeat it for the actual sample side

³Allresist AR 600-55, diluted 1:2 with isopropanol

⁴Allresist AR 600-60

2. Blow off the sample with N_2 to remove glass shards and dust
3. Fixate the substrate on the spin coater
4. Drench one side of a cotton swab with acetone
5. Set the spin coater to 4000 rpm for 20 s. Then clean the rotating substrate by moving across the surface, but stay away from the edge.
6. When the spin coater has come to a stop, hold the substrate to keep it from turning and move the swab along its edges
7. Drench another swab and shake it thoroughly to remove any excess acetone.
8. Move across the inner area of the substrate with parallel strokes.
9. Check the substrate in a dark field microscopy setup and repeat if necessary.

A.2. Sample characterization

A.2.1. Determination of nanodisk diameter

The nominal nanodisk diameters used to fabricate the sample for the transmission spectroscopy measurement in section 4.2 and the single particle scattering spectroscopy in Fig. 4.15 and Fig. 4.16 are 100–300 nm. To estimate the nanodisk sizes, SEM images of 7 nominally identical nanodisks are taken and measured from line plots across the SEM images. The averaged results are plotted with the respective standard deviations in Fig. A.1 a), and listed in table A.1. The variations between nominally identical nanodisks are related to an uncertainty of the measurement caused by the nanodisk's edge roughness and due to a distribution of the actual nanodisk sizes. The differences between averaged diameters and nominal diameters are plotted in Fig. A.1 b). The differences are only weakly dependent on the nanodisk diameter. The average value (of all measured nanodisks) of the offset is 16.3 nm with a standard deviation of 4.3 nm. To facilitate the description we round to 15 nm and estimate an uncertainty of ± 7 nm. This value is used to correct the nanodisk diameters in the simulations and to label the nanodisks in the measurements. From SEM measurement of the remaining samples fabricated with the same parameters, it can be seen that this difference of $15 \text{ nm} \pm 7$ is justifiable as well.

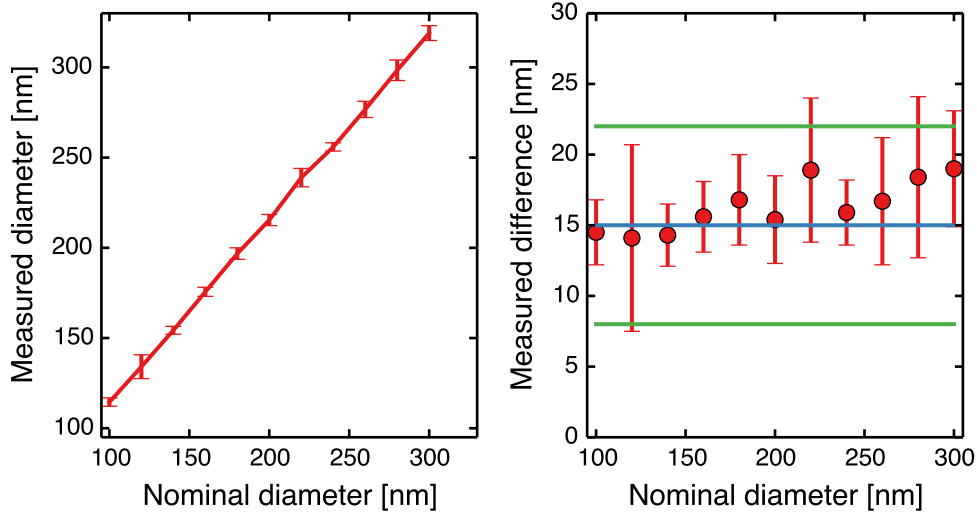


Figure A.1.: a) Measured mean nanodisk diameters over nominal diameters. b) Difference between nominal diameter and measured diameter. The blue line is the assumed constant offset of 15 nm and the green lines mark show the assumed uncertainty of ± 7 nm.

A.2.2. Estimation of the number of quantum dots

Here, the goal is to estimate the number of QDs in the patches on the silver nanodisks. This will be done with SEM images of the positioned QDs and TEM images of a QD monolayer. The QDs are positioned on the silver nanodisks by deposition into holes in the PMMA exposed with a *dot dose* of 20 fC.

From SEM images (see Fig. 5.2)) the diameter of the QD patches is estimated to be 65 ± 5 nm in diameter. Figure A.2 shows a TEM image of the used QDs. From three different areas in the image, the average area of one

Table A.1.: Comparison of nominal nanodisk diameters d_{nom} with the measured values of real nanodisks d . The table includes the mean nanodisk diameter $\text{mean}(d)$ and the standard deviation $\text{std}(d)$.

d_{nom}	100	120	140	160	180	200	220	240	260	280	300
$\text{mean}(d)$	114	134	154	176	197	215	239	256	277	298	319
$\text{std}(d)$	3	7	4	3	4	4	6	3	5	5	5

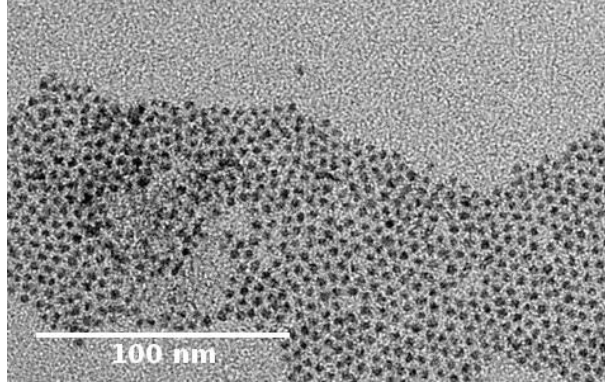


Figure A.2.: TEM image of a monolayer of CANdot core/shell/shell QDs. From Ref. [46].

QD is estimated to be $A_{\text{TEM}} / N_{\text{TEM}} = 27 \pm 1 \text{ nm}^2$. By dividing the area of the QD patches by the area of a single QD, we estimate 100–150 QDs per single layer. However, from the SEM images in Fig. 5.2, we expect multiple layers. Furthermore, the filling varies from position to position. This means that this number is only a rough estimation.

If we assume hexagonal packing, an effective diameter d_{QD} of the QDs can be calculated from the TEM images:

$$A_{\text{QD}} = \left(\frac{d_{\text{QD}}}{2} \right)^2 \pi = \frac{\pi}{2\sqrt{3}} \frac{A_{\text{TEM}}}{N_{\text{TEM}}}, \quad (\text{A.1})$$

where A_{QD} is the area of one (circular) QD, $\frac{\pi}{2\sqrt{3}}$ is the hexagonal packing density, A_{TEM} and N_{TEM} are the area and number of QDs, respectively, as measured by TEM. The resulting effective diameter is $d_{\text{QD}} = 5.6 \text{ nm}$. This is an estimation of the effective diameter of each QD with its organic molecule around. According to the supplier, the diameter of the nanocrystal alone is $2.7 \pm 0.4 \text{ nm}$ [46].